



Science Arts & Métiers (SAM)

is an open access repository that collects the work of Arts et Métiers Institute of Technology researchers and makes it freely available over the web where possible.

This is an author-deposited version published in: <https://sam.ensam.eu>
Handle ID: <http://hdl.handle.net/10985/17799>

To cite this version :

Paul ZEHNER, Fabrice FALISSARD, Xavier GLOERFELT - Aeroacoustic Study of the Interaction of a Rotating Blade with a Batchelor Vortex - AIAA Journal - Vol. 56, n°2, p.629-647 - 2018

Any correspondence concerning this service should be sent to the repository

Administrator : scienceouverte@ensam.eu



Aeroacoustic Study of the Interaction of a Rotating Blade with a Batchelor Vortex

P. Zehner*

ONERA–The French Aerospace Lab, 92322 Châtillon, France

F. Falissard†

ONERA–The French Aerospace Lab, 92190 Meudon, France

and

X. Gloerfelt‡

Arts et Métiers ParisTech, 75013 Paris, France

The aeroacoustic response of the orthogonal interaction of a rotating blade with an isolated Batchelor vortex is studied by means of numerical simulation. The relative influence of the vortex tangential and axial velocity on the blade aerodynamics and on the acoustics radiated in the far field is analyzed by comparing the interaction with a Batchelor vortex to the interactions considering the vortex tangential or axial velocity components. Analyses show that the vortex tangential velocity contributes mostly to the noise level at low frequencies, whereas the vortex axial velocity is responsible for the contribution at high frequencies. For the range of frequencies in between, the interaction noise results from constructive interferences of the noise radiated separately by each velocity component of the vortex.

Nomenclature

A	=	axial parameter
A'	=	adapted axial parameter
BPF	=	blade-passing frequency, Hz
C	=	blade chord, m
C_p	=	pressure coefficient
C_T	=	thrust coefficient
C'_T	=	adapted thrust coefficient
C_T^{\max}	=	amplitude of the thrust coefficient
D_t	=	propeller diameter, m
I	=	impact parameter
J	=	blade advance ratio
L	=	mesh part size, m
l	=	mesh cell size, m
M_h	=	blade helical Mach number
M_t	=	blade tip rotational Mach number
N	=	blade angular frequency, Hz
p	=	pressure, Pa
q	=	swirl number
q^{\min}	=	minimal admissible swirl number
R_i	=	blade/vortex interaction radius, m
R_r	=	blade root radius, m
R_t	=	blade tip radius, m
r_c	=	vortex core radius, m
T	=	thrust, N
v_a	=	vortex axial velocity deficit, $\text{m} \cdot \text{s}^{-1}$
v_a^{\max}	=	vortex axial velocity deficit amplitude, $\text{m} \cdot \text{s}^{-1}$
v_a^{MAX}	=	maximal admissible vortex axial velocity deficit amplitude
$v_a^{*\max}$	=	dimensionless vortex axial velocity deficit amplitude

v_g	=	gust velocity vector seen by the blade, $\text{m} \cdot \text{s}^{-1}$
v_h	=	blade helical velocity, $\text{m} \cdot \text{s}^{-1}$
v_r	=	vortex radial velocity, $\text{m} \cdot \text{s}^{-1}$
v_t	=	blade tip velocity, $\text{m} \cdot \text{s}^{-1}$
v_u^*	=	dimensionless relative blade upwash velocity
v_x	=	vortex axial velocity, $\text{m} \cdot \text{s}^{-1}$
v_θ	=	vortex tangential velocity, $\text{m} \cdot \text{s}^{-1}$
v_θ^{\max}	=	vortex tangential velocity amplitude, $\text{m} \cdot \text{s}^{-1}$
$v_\theta^{*\max}$	=	dimensionless vortex tangential velocity amplitude
α	=	vortex radius correcting factor
β	=	blade relative angle of attack with the gust, deg
γ	=	gas specific heats ratio
Γ	=	vortex circulation, $\text{m}^2 \cdot \text{s}^{-1}$
Δv	=	vortex core axial velocity deficit, $\text{m} \cdot \text{s}^{-1}$
Δv_i^*	=	dimensionless relative amplitude of the gust
θ	=	blade azimuth angle, deg
ρ	=	density, $\text{kg} \cdot \text{m}^{-3}$
σ	=	blade thickness, m
τ	=	thickness parameter
ω	=	blade azimuth angular speed, $\text{rad} \cdot \text{s}^{-1}$
\sim	=	fluctuating value
$-$	=	average value

Subscript

∞	=	upstream flow value
----------	---	---------------------

I. Introduction

THE aeronautic industry focuses on decreasing its environmental footprint as well as increasing airplanes efficiency. One way is to design more efficient engines, such as counter-rotating open rotors. Open rotors have higher efficiency than turboprops of equal power but generate more noise due to the absence of casing. This noise results from the front and rear rotors self-noise and from the aerodynamic interactions of both rotors. The highest contribution to this interaction noise at low speed (typically takeoff or landing flight condition) is the orthogonal interaction between the blades of the rear rotor and the tip vortices generated by front rotor blades. This phenomenon also occurs when a propeller is mounted behind a wing and interacts with the vortices created by its high-lift devices or ruddervators.

Early works have been conducted in the context of helicopter applications to study the orthogonal interaction that occurs between the tip vortices generated by the main rotor and the blades of the tail rotor. Schlenger and Amiet [1] used a simplified setup where a steady

*Ph.D. Student, Aerodynamics, Aeroelasticity and Acoustics Department; paul.zehner@onera.fr. Member AIAA (Corresponding Author).

†Research Scientist, Aerodynamics, Aeroelasticity and Acoustics Department; fabrice.falissard@onera.fr. Member AIAA.

‡Professor, DynFluid Laboratory; xavier.gloerfelt@ensam.eu.

streamwise tip vortex generated by an upstream airfoil interacts with a model rotor whose rotational disc is orthogonal to the flow. Their interaction is representative of the one encountered for a propeller, with the main noticeable difference being the absence of twist law for the rotating blades. First, characteristics of the incoming vortex were obtained using hot-wire anemometry. The authors observed a nonnull axial velocity within the vortex along with its tangential velocity component. The visualized trajectory was affected by the vena contracta effect due to the rotor aspiration. This yielded a modified angle between the vortex and the blade disc, making the interaction not rigorously orthogonal. The radiated noise was measured on an arc of microphones and indicated a directivity pattern with a dipolar shape from 5 to 21BPF, which is the maximal frequency their hardware could record. Schlinker and Amiet [1] noticed a weak influence of the vortex axial velocity deficit on the interaction noise. It is, however, worth noting that the amplitude of the axial velocity was five times smaller than the one of the tangential velocity, and its effect could be masked by the background noise. Ahmadi [2] and Cary [3] have conducted further experiments based on the same setup focusing on the fluctuating pressure on the blade. However, due to the blade motion, only four pressure probes could be installed on the blade surface, implying a limited pressure field resolution. They observed that the pressure fluctuations had a higher amplitude above the interaction radius on the pressure side than on the suction side and conversely a higher amplitude below the interaction radius on the suction side than on the pressure side. They also identified that the directivity pattern remains dipolar as long as the interaction occurs away from the blade tip. Nonetheless, a further characterization was made difficult because the vortex parameters before the chopping were not fully known. Howe [4,5] proposed an analytical model for the interaction of a vortex with a translating flat blade. His model, based on vortex sound theory valid at low Mach numbers, states that a strict orthogonal interaction between a tangential vortex and a blade does not produce any noise. The adjunction of a finite axial velocity component will generate a dipolar sound. Howe [4] compared qualitatively the modeled pressure signature with the experimental results of Schlinker and Amiet [1] and discussed the additional trailing-edge noise source due to the blade wake. Roger et al. [6,7] and Quaglia et al. [8,9] derived a new analytical model based on Amiet's theory [10]. They considered a translating flat plate, with an infinite or finite length, interacting with different vortex models including or not an axial velocity component. The dimensionless swirl number q , defined as the ratio between the vortex tangential and axial velocities, was used to characterize the vortex. For a purely tangential vortex and an infinite blade, the upwash due to the interaction generates noise with a quadripolar directivity. Roger et al. [7] showed that the finiteness of the blade results in a dipolar radiation if the interaction occurs close to the blade tip, which confirm the early observations of Schlinker and Amiet [1]. A dipolar pattern also appeared when the interaction occurs on the blade tip, but its lobes are oriented toward the blade axis. An axial component was seen to induce an additional dipolar noise. Quaglia et al. [8,9] investigated 3-D effects and showed that a modification of the incidence angle due to the vena contracta has the same effect as imposing a sweep angle to the blade.

Regarding the orthogonal blade/vortex interaction occurring on open rotors, Vion [11] and Delattre and Falissard [12,13] have conducted experimental and numerical studies on ONERA–The French Aerospace Lab's HTC5 open rotor. The simulations involved a front propeller whose blades generate tip vortices that interact with the rear propeller blades. According to the incident tip vortices obtained in the simulations, they suggest that the influence of the axial velocity component may contribute significantly to the noise. However, these studies showed that working on realistic blade geometries is too complex to analyze the influence of each parameter individually.

Extensive studies on the dynamics of the interaction have been motivated by helicopters applications [14]. The investigations of Marshall et al. [15–18], Krishnamoorthy and Marshall [19], Liu and Marshall [20], and Filippone and Afgan [21] considered a simplified configuration to shed new light on the physics of the orthogonal

interaction. The case of a fixed vertical vortex cut by a horizontal translating blade was studied by experimental, numerical, and analytical means. These authors introduced several dimensionless parameters to characterize the vortex response: the impact parameter I (ratio between the blade impact velocity on the vortex and the vortex tangential velocity), the axial flow parameter A (ratio between the axial and tangential velocity components of the vortex), and the thickness parameter noted hereafter τ (ratio between the blade thickness and the vortex core radius). Small values of the impact parameter correspond to the strong-vortex regime, where the vortex rotation is high enough to eject vorticity from the boundary layer developing from the blade leading edge and brings it into the rotating motion. On the other hand, high values correspond to the weak-vortex regime, where the blade penetrates the vortex core without separation of the boundary layer. In this case, the thickness parameter determines the shape of the vortex during the impact on the blade body. The vortex tube is considerably deformed for high values of this parameter, whereas its shape is almost not altered for low values. These authors observed that the axial velocity component creates a variation of the vortex core radius as the vortex is cut by the blade. This effect is characterized by the axial flow parameter A . Below a given limit, the vortex is termed subcritical, where the blocking effect due to the blade induces perturbations of the vortex section that propagate along the vortex tube both in the upstream and downstream directions (relative to the direction of the axial component). The radius increases on the upstream side of the vortex (compression waves), whereas it decreases on the downstream side (expansion waves). Above the limit, the vortex is termed supercritical. The behavior on the compression side is then similar to a jet impacting a wall. The adjunction of an axial velocity in the vortex core thus makes the flow disymmetric and leads to a nonnull thrust on the blade. The amplitude of the normal forces on the blade appears to be proportional to the axial velocity deficit amplitude. Marshall et al. noticed that the Reynolds number has little influence on the interaction. Yildirim and Hillier [22] investigated a simpler case involving the simulation of a vortex with axial and tangential velocities instantaneously cut by a blade. The study focused on the influence of the compressibility of the flow and proposed comparisons with the model of Marshall [15]. They adapted the axial parameter, noted hereafter A' , which is the ratio between the averaged vortex axial velocity deficit and the tangential velocity amplitude. They used the criterion $A' \leq 1/\sqrt{2}$ for subcritical vortices and supercritical otherwise. The compressibility effects were limited to the compression side for subcritical vortices and produced a damped wave effect on the vortex core radius. Doolan et al. [23–25], stating that the early studies of Schlinker and Amiet [1], Ahmadi [2], and Cary [3] were not representative of a realistic helicopter situation, investigated the interaction from a different point of view. They developed an experimental apparatus for a horizontal wind tunnel where a single blade rotated around a vertical axis and generated a vortex with a cycloid shape. The vortex was advected and cut by a fixed and untwisted NACA 0015 blade placed downstream, whose chord was streamwise. The location of the incident blade was chosen so as to have an orthogonal interaction. Vortex features were gathered through hot-wire and particle image velocimetry measurements. They reported in particular that the amplitude of the axial velocity deficit in the core was of similar amplitude as the vortex tangential velocity. The incident blade was equipped with a line of 30 pressure probes placed at 78.5% of the blade span. Doolan et al. observed the passing of the vortex on the blade for several angles of incidence. For the whole angle range, they observed that the vortex produced a local suction on the upper surface of the blade and a local pressure rise on the lower surface. The amplitude of these pressure variations was maximal at the leading edge. Moreover, the maximal normal force on the blade was obtained as the vortex impacted the blade, which was interpreted as an effect of the vortex axial velocity.

The aforementioned studies have shown that the orthogonal blade/vortex interaction is a complex phenomenon. Several of its aspects have been analyzed on the basis of the blade (pressure distribution, forces), of the vortex (vortex deformation), or of the radiated noise (acoustic signatures, sound levels, directivity patterns) by varying

blade or vortex parameters. In particular, the tip vortices exhibit an axial velocity deficit with various amplitudes. Most of the works cited had, however, no control on this parameter, except in the analytical studies, which makes its influence not known in details. Consequently, the aim of this paper is to investigate and better qualify the relative influence of this axial velocity. We investigate the interaction between a rotating blade of simplified geometry and a Batchelor vortex, representative of a realistic tip vortex, which includes an axial velocity deficit. This study has been conducted by numerical means, using an inviscid flow assumption.

The paper is organized as follows. Section II presents the numerical experiments, the blade geometry and kinematics, the vortex model, and the numerical values chosen for the parameters that drive the intensity of the blade/vortex interaction. Section III presents the numerical setup used for the CFD and noise radiation computations, the methodology, and the discretization grids and numerical schemes. The results are presented and analyzed in Sec. IV. First, the orthogonal interaction of a rotating blade with a Batchelor vortex is considered. Then, the computations are carried out for the orthogonal interaction with a Lamb–Oseen vortex and with a Gaussian axial velocity deficit, respectively, to investigate separately the role of the tangential and axial components of the incoming vorticity. An extra case was computed without any vortex to measure the background noise due to the numerical setup. Then, the analyses of the three computed interactions are put together to identify the influence of each parameter on the noise radiated by the blade vortex interaction. Finally, variations on this reference case are conducted and analyzed by considering different ratios of tangential to axial components.

II. Numerical Experiment

This paper focuses on the interaction between a single rotating blade and an isolated Batchelor vortex, as depicted in Fig. 1. The numerical setup, described hereafter, relies on a methodology developed in previous papers [26–28].

A. Blade Geometry and Kinematics

The straight blade is described in the cylindrical coordinate system (u_r, u_θ, u_x) . It has a tip radius $R_t = 1$ m and a root radius $R_r = 0.2R_t$. The blade section is a NACA 0002 airfoil, with a sharp trailing edge, of thickness noted σ and of chord $C = 0.2R_t$. The blade rotates around the x axis and is twisted around its leading edge such that the kinematic angle of attack of all blade sections is null for an upstream Mach number $M_\infty = 0.25$ and a tip rotation Mach number $M_t = 0.65$. This corresponds to a helical tip Mach number $M_h = \sqrt{M_\infty^2 + M_t^2} \approx 0.696$ and an advance ratio $J = v_\infty/(ND_t) \approx 1.21$, where N is the blade angular frequency, and $D_t = 2R_t$ is the propeller diameter.

B. Vortex Model

The blade interacts with a rectilinear vortex, the axis of which is parallel to the blade rotation axis x . Its core radius is $r_c = C/8 = 2.5 \times 10^{-2}R_t$. The vortex intersects the blade at the interaction location $(0, 0, R_i)$ with $R_i = 0.9R_t$.

The vortex model used for the interaction is a Batchelor vortex [29,30], or q -vortex. Thanks to its axial and azimuthal components, this vortex represents a good approximation of the trailing vortices [30]. The vortex velocity field is written as

$$v_r = 0 \quad (1)$$

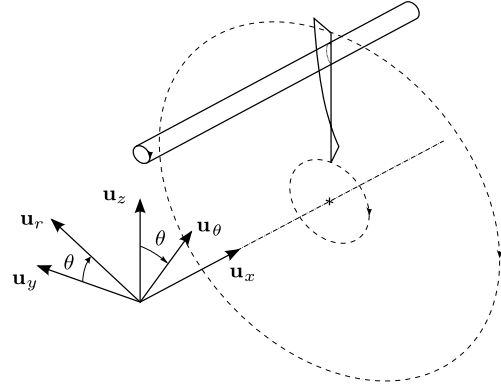


Fig. 1 Scheme of the blade/vortex interaction.

$$v_\theta = \frac{\Gamma}{2\pi r} (1 - e^{-\tilde{r}^2}) \quad (2)$$

$$v_x = v_\infty + \Delta v e^{-\tilde{r}^2} \quad (3)$$

where $\tilde{r} = r/r_c$ is the dimensionless radius, Γ is the vortex circulation, v_∞ is the upstream flow velocity along the x axis, and Δv is the velocity deficit, which is the difference between the maximal streamwise velocity at the vortex core and the upstream flow velocity. The velocity field defined by Eq. (2) does not reach its maximum for $\tilde{r} = 1$, but for $\tilde{r} = \alpha$, where α is solution of the equation $2\alpha^2 + 1 - e^{\alpha^2} = 0$ and takes the numerical value $\alpha \approx 1.121$. It is possible to express the tangential velocity field as a function of the maximum velocity v_θ^{\max} reached at $\tilde{r} = 1$ and the axial velocity as a function of v_a^{\max} :

$$v_\theta = v_\theta^{\max} \frac{1 - e^{-\alpha^2 \tilde{r}^2}}{\tilde{r}(1 - e^{-\alpha^2})} \quad (4)$$

$$v_x = v_\infty - \underbrace{v_a^{\max} e^{-\tilde{r}^2}}_{v_a} \quad (5)$$

The azimuthal velocity v_θ and axial velocity v_x depend on \tilde{r} only, with the circulation Γ and the velocity deficit Δv being the main parameters of the vortex. Because the simulations are carried out using the Euler equations, density and pressure fields need also to be calculated. To this aim, the continuity and momentum equations of the three-dimensional compressible Euler equations are used, in the cylindrical coordinate system (r, θ, x) . Under the assumptions of a stationary axisymmetric flow with such a vortex, which is x -invariant and has no radial velocity component, the radial equilibrium equation is obtained:

$$\frac{dp}{dr} - \rho \frac{v_\theta^2(r)}{r} = 0 \quad (6)$$

An additional hypothesis on the flow is needed to close the system. We retain here an homentropic assumption, $p/\rho^\gamma = p_\infty/\rho_\infty^\gamma$, for which the pressure field has been given by Colonius et al. [31] as

$$\frac{p}{p_\infty} = \left(1 - \frac{\gamma-1}{\gamma} \frac{p_\infty}{\rho_\infty} \left(\frac{v_\theta^{\max}}{1 - e^{-\alpha^2}} \right)^2 \left(\frac{(1 - e^{-\alpha^2 \tilde{r}^2})^2}{2\tilde{r}^2} + \alpha^2 (\text{Ei}(-2\alpha^2 \tilde{r}^2) - \text{Ei}(-\alpha^2 \tilde{r}^2)) \right) \right)^{\gamma/(\gamma-1)} \quad (7)$$

where Ei is the exponential integral function.

C. Blade/Vortex Interaction Parameters

The Mach number of the upstream flow corresponds to a takeoff or beginning of climb flight condition. For UAVs or business aircraft with a rear-mounted propeller, ruddervators or high-lift devices are likely to be activated, leading to blade/vortex interaction similar to those depicted in Figs. 2a and 2b, resulting in an increase of radiating noise. For open rotors, this operating point leads to high-level of noise resulting from the interaction of the front rotor tip vortices on the rear rotor, as in Fig. 2c.

To be representative of a realistic interaction occurring on open rotors, vortex parameters have been chosen according to previous experimental [11] and numerical [12,32] studies carried out on ONERA's HTC5 generic open rotor [33], which is intensively used for fundamental research studies. The most detailed measurements are provided by the work of Vion, which addresses the influence of the front rotor blade geometry on the tip vortex characteristics [11] and its modification to reduce interaction noise [32]. Her experiments featured a single fixed blade, with a modified twist law so as to reproduce the behavior of an open rotor blade. Numerical data were also obtained by Reynolds averaged Navier–Stokes (RANS) computations reproducing the experiments. Detailed characteristics of front rotor tip vortices are also given by Delattre and Falissard [12] in a study addressing the influence of the torque ratio between the front and rear rotors on the interaction noise at takeoff condition. Four distinct operating points were simulated using unsteady RANS computations, giving the detailed characteristics of the front rotor tip vortices for different values of the rotor thrust. The analysis concluded that decreasing the strength of the front rotor tip vortices leads to a reduction of the noise but could not determine whether this acoustic gain was due to the lowering of the tangential or axial velocity component of the vortex. The vortex parameters extracted from the studies mentioned previously are presented in Fig. 3 and in Table 1.

Figure 3 sorts the different vortex tangential and axial velocity magnitudes in the parametric space $(v_{\theta}^{*max}, v_a^{*max})$ for the aforementioned studies. Note that these magnitudes have been nondimensionalized by a reference velocity adapted to our study, which is the relative velocity magnitude in the blade reference frame,

Table 1 Comparison of swirl-number ranges of vortices with previous studies

Study	Swirl number q	
	Minimum	Maximum
Delattre and Falissard [12] (CFD)	0.579	1.180
Vion [11] (experiment)	0.321	0.964
Vion [11] (CFD)	0.587	0.800
Schlinker and Amiet [1] (experiment)	5.278	5.278
Doolan et al. [24] (experiment)	1.113	1.113
Present study (CFD)	0.850	2.000

or helical velocity $v_h = (v_{\infty}^2 + (R_t\omega)^2)^{1/2}$. This leads to nondimensional values different from the ones given in the original papers in which the reference velocity is usually the upstream velocity. Using the helical velocity as reference velocity, most of the vortices characterized in the cited studies have dimensionless maximum tangential velocity between 0.2 and 0.34 and dimensionless maximum axial velocity deficit between 0.2 and 0.7. Consequently, we have chosen to set v_{θ}^{*max} for this study to 0.25. We can also compare the different vortices by calculating the swirl number q , defined as

$$q = \frac{v_{\theta}^{max}}{v_a^{max}} \quad (8)$$

Table 1 lists the minimal and maximal swirl numbers of the vortices used in each study. The swirl number of most vortices stands between 0.3 and 1. For the numerical experiment of the present paper, the upstream flow and the vortex axis are collinear. This has a consequence on the range of swirl numbers that can be simulated because the axial velocity in the vortex core must remain positive. Following this constraint, because of the upstream velocity, the helical velocity, and the maximum tangential velocity chosen in this study, the smallest admissible swirl number is $q^{MIN} = (1/4)v_h/v_{\infty} \approx 0.696$, and the largest admissible maximum axial velocity deficit is $v_a^{MAX} = v_{\infty} \approx 0.359v_h$. Three different

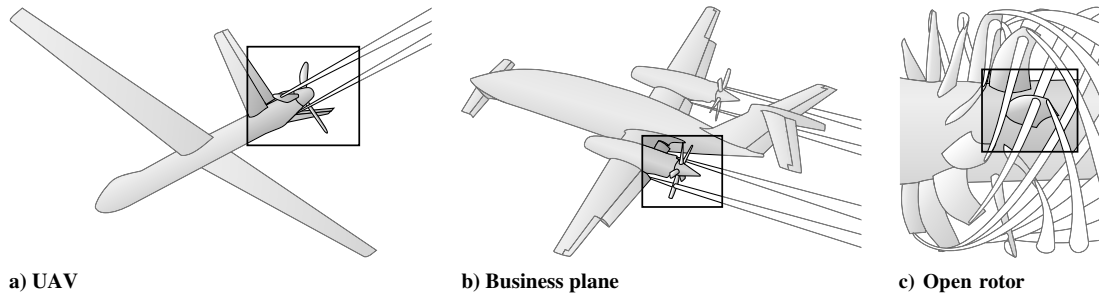


Fig. 2 Blade/vortex interaction occurrences for different plane configurations.

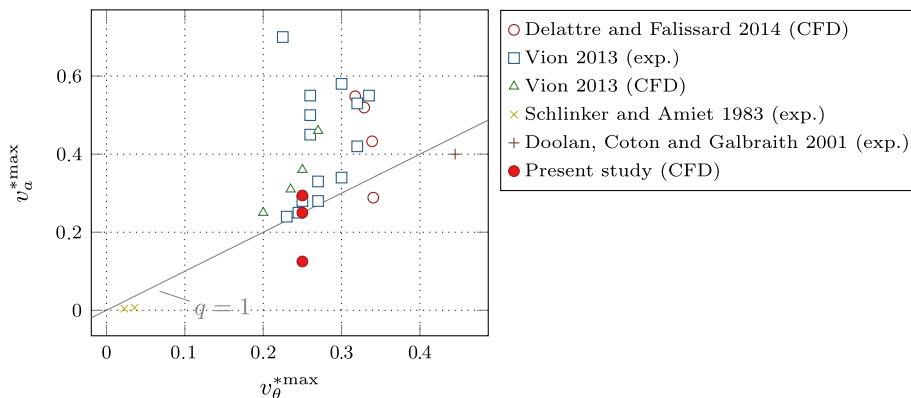


Fig. 3 Comparison of tangential and axial velocities of vortices with previous studies.

Table 2 Dimensionless parameter of the blade/vortex interaction

Swirl number q	Impact parameter I	Axial parameter A'	Thickness parameter τ
0.85	3.360	0.618	0.16
1	3.360	0.525	0.16
2	3.360	0.263	0.16

swirl numbers for this study will be considered: 0.85, 1, and 2. The reference case being the unitary swirl number corresponding to $v_{\theta}^{\max} = v_a^{\max} = (1/4)v_h$.

To relate the selected with earlier studies, we have added in Fig. 3 and in Table 1 the values of the vortices reported by Schlinker and Amiet [1] and by Doolan et al. [25]. The dimensionless parameters defined by Marshall and Krishnamoorthy [18] to characterize the orthogonal blade/vortex interaction can be adapted for this interaction configuration. Hence, the impact parameter I is the ratio between the blade velocity at the interaction radius and the vortex tangential velocity amplitude:

$$I = \frac{2\pi r_c \omega R_i}{\Gamma} = \frac{v_t R_i}{v_{\theta}^{\max} R_i} \quad (9)$$

The axial parameter A' , as adapted by Yildirim and Hillier [22], is the ratio of the mean vortex axial velocity deficit and the tangential velocity amplitude:

$$A' = \frac{2\pi r_c \bar{v}_a}{\Gamma} = \frac{\bar{v}_a}{v_{\theta}^{\max}} = \frac{\bar{v}_a}{v_a^{\max}} \frac{1}{q} \quad \text{with} \quad \bar{v}_a = \frac{1}{\pi r_c^2} \int_0^{r_c} 2\pi r v_a(r) dr \quad (10)$$

where \bar{v}_a/v_a^{\max} is constant for all cases, which allows us to show a clear dependency on the swirl number q . Then, the thickness parameter τ is

$$\tau = \frac{\sigma}{r_c} \quad (11)$$

These parameters are reported in Table 2 for the three selected values of the swirl number. We observe that, in the meaning of Marshall et al., for all cases, the interaction is of the weak-vortex regime, the vortex is subcritical, and the blade body should not alter the shape of the vortex. This justifies the use of Euler equations, where no boundary layers are accounted for.

III. Numerical Setup

The computational method relies on the coupling of high-order computational fluid dynamics (CFD) to compute the aerodynamic sources, with the Ffowcs Williams and Hawkins integral method, to propagate the noise in the far field. The computational meshes are built using Cassiopée tools [34], considering a near-body/off-body grid approach [34].

The blade near body is meshed using a two-block O-type curvilinear mesh and is extruded in the normal direction. The sketch of the blade mesh is plotted in Fig. 4, where black labels are related to the skin blade mesh, and gray labels are related to the extruded part of the mesh (which is partially displayed for readability). The different

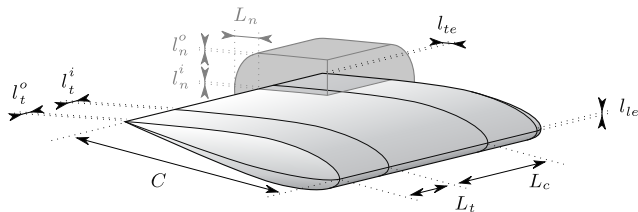


Fig. 4 Sketch of the blade mesh. The blade is unswirled and has a nonproportional shape for illustration.

Table 3 Sizes, cell lengths, and number of points in the near-body mesh

Symbol	Description	Size normalized by R_t	Points
R_t	Blade tip radius	1	—
R_r	Blade root radius	0.2	—
C	Chord	0.2	61
l_{le}	Leading edge cell	1×10^{-4}	—
l_{te}	Trailing-edge cell	1×10^{-3}	—
L_t	Tip span	0.1	47
L_c	Central part span	0.6	60
l_n^o	Tip outer cell	1×10^{-4}	—
l_n^i	Tip inner cell	1×10^{-2}	—
L_n	Extrusion length	0.1	53
l_n^o	Extrusion outer cell	5×10^{-3}	—
l_n^i	Extrusion inner cell	1×10^{-3}	—

sizes, cell lengths, and number of points used are detailed in Table 3. The airfoil geometry is discretized with a biexponential law. The blade span is divided in three parts: the blade tip, the blade central part, and the blade root. Blade tip and blade root are similarly designed, ending with elliptic edges of ratio 1/2. They are meshed using a geometric law in the spanwise direction. The central part of the blade, between the blade tip and the blade root, is uniformly meshed. The total blade span is discretized with 152 points. This skin mesh is extruded in the normal direction and smoothed with a Laplacian filter to avoid sharp cells at the leading and trailing edges. The resulting blade mesh is about 1 million points. Figure 5 shows a slice of this mesh in the plane normal to $r = R_t$. The blade is then located in the computational domain, with an initial azimuth of $\theta_0 = -225$ deg.

This blade mesh rotates in a fixed off-body mesh built from an octree of Cartesian meshes of different refinement densities [35] adapted to the simulation and defined by refinement areas. The dimensions of the octree and its areas are illustrated in Fig. 6; the density is high in the areas of the vortex and of the blade and then gradually decreases up to the computational domain boundaries. Two slices of the generated mesh are presented in Fig. 7; Figs. 6a and 7a represent the mesh in the plane $x = 0$ and Figs. 6b and 7b in the plane $y = 0$. The different cell sizes in the refinement areas are given in Table 4.

In the x plane, the off-body mesh is refined near the blade area and particularly close to the vortex area, where 20 points are used to discretize the vortex core diameter. In the y plane, the mesh density in the last third of the computational domain in the x dimension is lowered to reduce pressure and velocity disturbances at the outlet boundaries. Each Cartesian mesh has an interpolation overlap of two cells. The total mesh involves about 37 million points and is displayed with the vortex in Fig. 8b. The different meshes used are coupled using the Chimera method [36,37].

The noise radiated by the blade/vortex interaction is computed for 1944 probes on a sphere of radius $R_p = 20R_t$. The maximal angle between two probes is 5 deg. Figure 8c displays this network together with the computational domain.

The aerodynamic model relies on the three-dimensional compressible Euler equations. A compressible solver is used because of the tip Mach number value, which is 0.65. CFD computations are performed using Cassiopée's high-order solver, with a spatial discretization scheme of third-order accuracy on

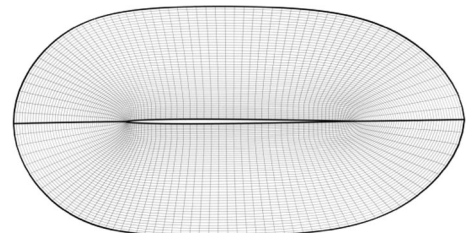


Fig. 5 Near-body mesh slice, plane normal to $r = R_t$.

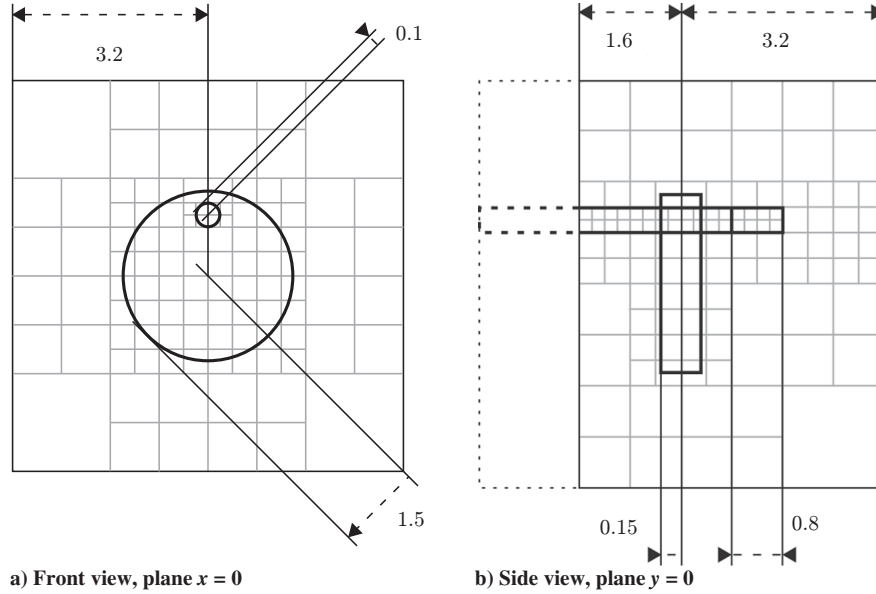


Fig. 6 Sketch of the off-body octree dimensions. Sizes normalized by R_t .

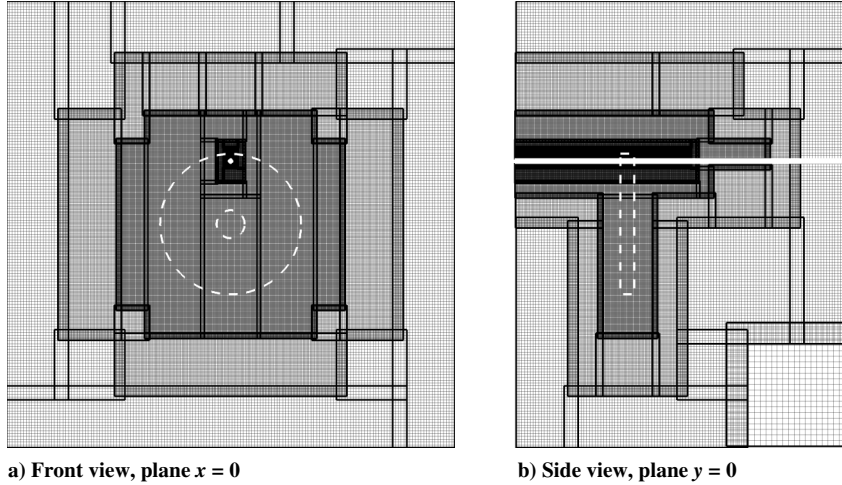


Fig. 7 Off-body mesh slices; the white dashed shape represents the blade position over azimuth, and the white dot and line represent the vortex core.

curvilinear meshes and fifth-order accuracy on Cartesian meshes [38,39]. The Chimera interpolations are of second-order accuracy. The time integration uses a second-order three-time-level backward differencing formula, which is implicit and solved by a Newton's algorithm. The blade has a wall slip boundary condition. The face of the off-body mesh in the upstream direction has an inlet boundary condition and injects the upstream flow with the vortex. The other faces have a far-field boundary condition. Each computation is first initialized with the same values as the inlet boundary condition. A preliminary steady computation of 10,000 iterations is performed and is subsequently used as the initialization field for the unsteady computation. This computation is performed for 2.25 rotations of the blade, with a time step corresponding to 0.25 deg of the blade rotation, which is about 6.713×10^{-3} s. The azimuth 0 deg corresponds to the first time the blade crosses the interaction location. To discard the transitory phase due to the flow initialization, all the

acoustic computations and postprocessing have been performed during the second rotation of the blade, in the azimuth interval from 180 to 540 deg, which corresponds to 1440 iterations.

The aeroacoustic integral method relies on the Ffowcs Williams and Hawkings equation [40], in its rotating solid surface formulation, as implemented in the KIM solver [41]. The solid surface is the blade in rotation, during its last rotation. To get rid of the thickness and mean loading noise, a fluctuation pressure on the blade is computed: $p_f = p - \bar{p}$, with \bar{p} defined by the mean pressure on the blade surface over the last rotation. This means that only the fluctuating loading noise is observed. The aeroacoustic simulation results are then analyzed in the Fourier space for 100 frequencies that are multiples of the blade-passing frequency (BPF ≈ 35.7 Hz).

IV. Results and Discussion

For each value of the swirl number, three unsteady computations have been carried out to study and analyze the aerodynamic and aeroacoustic responses of the interaction. The first computation consists of the interaction of the blade with a Batchelor vortex including both tangential and axial velocity components. Two additional computations are used to separate the effect of the tangential velocity field only (Lamb–Oseen vortex [42–45]) and the axial velocity deficit only (Gaussian velocity deficit).

Table 4 Cell sizes in the off-body mesh

Area	Cell size normalized by R_t
Blade	1×10^{-2}
Vortex upstream	2.5×10^{-3}
Vortex downstream	1×10^{-2}

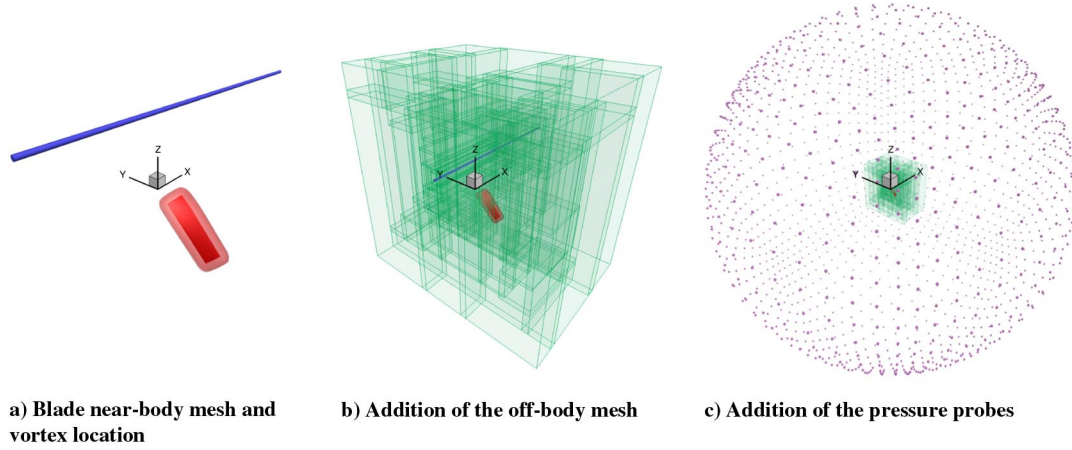


Fig. 8 Elements of the computational setup.

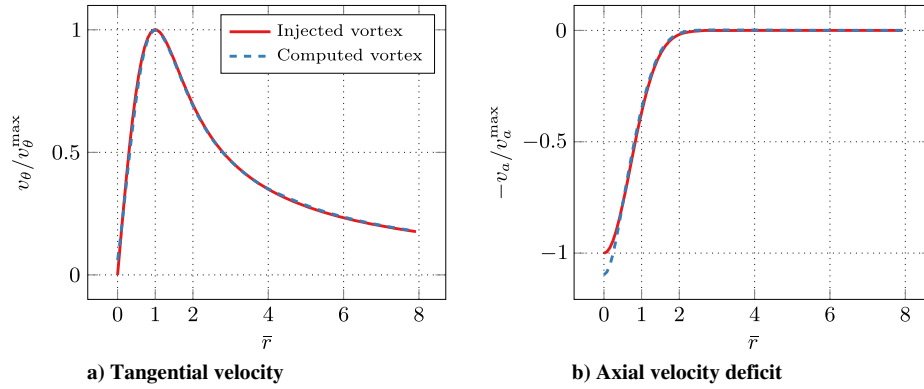


Fig. 9 Batchelor-vortex velocity profiles at the interaction location.

A. Interaction with a Batchelor Vortex

The Batchelor vortex interacting with the blade, defined by the Eqs. (4) and (5), exhibits identical absolute values of maximal tangential velocity and axial velocity deficit (i.e., Batchelor vortex with swirl number $q = 1$). According to previous studies on open rotor tip vortex characteristics, described in Sec. II, these amplitudes have been set to

$$v_{\theta}^{\max} = v_a^{\max} = \frac{1}{4} \sqrt{v_{\infty}^2 + (R_t \omega)^2} \quad (12)$$

The azimuthal and axial velocity components of the vortex, plotted in Fig. 9, have been interpolated from the steady computation at the location where the interaction occurs and are compared to the vortex injected at the inlet boundary condition. The interpolation is of second order and has been made along the segment $[(0, 0, R_t), (0, 0, R_t + 8r_c)]$ of 100 points. Such an interpolation is necessary because the center of the vortex is not located on a grid point.

For the vortex tangential velocity component, plotted in Fig. 9a, the computed and injected fields match very well for all values of \bar{r} . For the axial velocity deficit component, plotted in Fig. 9b, the injected and computed solutions are in good agreement for $\bar{r} \geq 0.5$. The amplitude for the computed solution in the vortex center is, however, 9.6% higher than expected. The origins of the variation of the axial velocity in the vortex core have been investigated and could result from disturbances due to the computational setup. It is indeed well known that the axial velocity field of the Batchelor vortex is very sensitive to small disturbances [46], which in our case are due to the flow deviation induced by the blade, the boundary conditions at the computational domain edges, and (last but not least) the different grid refinement levels along the vortex path.

Nonetheless, these results are rather good and indicate that the numerical setup is accurate enough to preserve the vortex up to the location of interaction with the blade.

The effect of the vortex impinging upon the blade can be observed through the thrust coefficient defined by $C_T = T / (\rho_{\infty} N^2 D_t^4)$, where D_t , the propeller diameter and T is the blade thrust. Figure 10 displays evolution of the fluctuation of the thrust coefficient as a function of the azimuthal angle, defined by $\hat{C}_T = C_T - \overline{C}_T$, where \overline{C}_T is the mean of the thrust coefficient over one rotation. The interaction with the blade is clearly visible for an azimuth close to 360 deg with a maximum thrust reached for an azimuth of about 363 deg. Even if the blade has been twisted so as to have a null angle of attack at the leading edge, a low but nonzero mean thrust ($\overline{C}_T \approx 4.898 \times 10^{-3}$) is generated. The influence of the vortex on the blade is felt for any azimuth, as illustrated by the wide base of the thrust pulse, due to the $1/r$ decay of the tangential velocity component. For an azimuth of

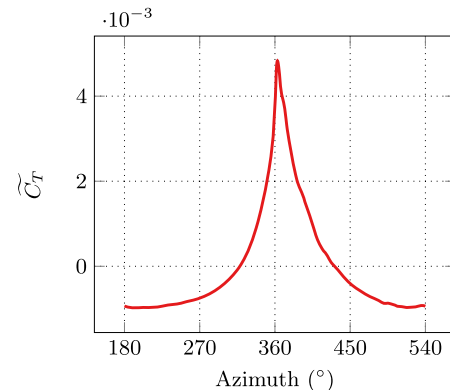


Fig. 10 Evolution of the fluctuation of the thrust coefficient as a function of the azimuthal angle for the interaction with a Batchelor's vortex.

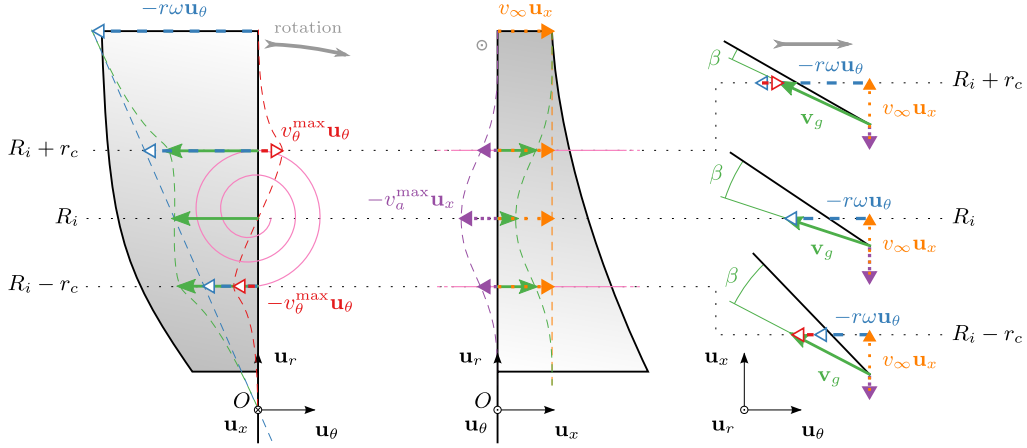


Fig. 11 Vortex alteration of the velocity field on the leading edge as seen by the blade for azimuth zero, from different angles.

180 and 540 deg (i.e., when the blade is opposite to the vortex), the velocity field induces a significant negative thrust fluctuation.

During the interaction, the vortex modifies entirely the flow seen by the blade. The use of a vortex model combining both tangential and axial velocity components results in a complex upwash that is sketched in Fig. 11 through projections of velocity triangles, for the blade at azimuth zero. The left view displays the velocities projected on the $(\mathbf{u}_r, \mathbf{u}_\theta)$ plane (propeller front view), the center view is on the $(\mathbf{u}_x, \mathbf{u}_r)$ plane (propeller side view), and the right view is projected on the $(\mathbf{u}_x, \mathbf{u}_\theta)$ plane (blade top view, when the blade azimuth is 0 deg). Because there is no radial velocity, the right view represents the velocity triangles correctly without projection. The amplitude of the different velocities and the vortex location in the figure have been magnified for illustration purposes. The locations of the three velocity triangles are respectively at the lower vortex core radius $r = R_i - r_c$, at the vortex center $r = R_i$, and at the upper vortex core radius $r = R_i + r_c$. It is worth noting that the presence of a nonnull upstream velocity in the same direction as the vortex axis makes the interaction not strictly orthogonal. As observed in the velocity triangles, the problem is a combination of orthogonal and perpendicular interactions.

The gust velocity vector \mathbf{v}_g as seen by the blade is written

$$\mathbf{v}_g(r) = \begin{pmatrix} 0 \\ -r\omega + v_\theta(r - R_i) \\ v_x(r - R_i) \end{pmatrix} \quad (13)$$

The magnitude of this gust velocity can be compared with the helical velocity, which is the velocity seen by the blade without any vortex. Let us define the relative magnitude Δv_i^* between these two velocities:

$$\Delta v_i^*(r) = \frac{\|\mathbf{v}_g(r)\| - v_h(r)}{v_h(r)} \quad (14)$$

The values of this relative magnitude along the blade span are plotted in Fig. 12a. Markers have been added at the lower vortex core radius, vortex center, and upper vortex core radius. We clearly see that there is an overspeed beneath the vortex center and an underspeed after. The relative velocity changes its sign very close to the vortex center, at about $r \approx 0.896R_i$. The extreme values of this dimensionless relative magnitude coincide with the vortex core and are about 0.23 for the overspeed and -0.30 for the underspeed.

The effect on the flow velocity magnitude is mixed with the effect on the angle of attack. In the right view of Fig. 11, we see that the velocity upwash, experienced by the blade during the interaction, generates locally strong variations of this angle. The resulting angle of attack β at a blade section of radius r is given by

$$\beta(r) = \arctan \frac{v_x(r - R_i)}{-(r)\omega + v_\theta(r - R_i)} - \arctan \frac{v_\infty}{-(r)\omega} \quad (15)$$

The variation of this angle along the blade span is plotted in Fig. 12b when the blade cuts the vortex. Markers have been added as before. The angle varies between 16 and -4.7 deg, which is not negligible, and the extremum value is reached close to the vortex center. The angle of attack is null at radius $r \approx 0.921R_i$. We can project the gust velocity on the blade orthogonal direction so as to get the dimensionless upwash velocity v_u^* , defined by

$$v_u^*(r) = \frac{\|\mathbf{v}_g(r)\| \sin \beta(r)}{v_h(r)} \quad (16)$$

The variation of this nondimensional velocity is plotted in Fig. 12c. The dimensionless upwash has the same sign as the relative angle β and has a similar fluctuation. The velocity is positive and increases gradually beneath the vortex core, then it reaches a maximum of 0.280 before the interaction radius at $r \approx 0.893R_i$. It decreases and reaches a minimum value of -0.074 at $r \approx 0.939R_i$. After this point, the velocity remains negative, and its amplitude decreases gradually.

These velocity variations have a consequence on the pressure distribution over the blade, as shown in Fig. 13, which displays the fluctuating pressure coefficient on the suction side of the blade, defined by $C_p = (p - \bar{p}) / ((1/2)\rho_\infty v_\infty^2)$, where \bar{p} is the mean pressure over one rotation. Dashed contour lines stand for negative values.

The figure shows the blade at several azimuths, from 360 deg (Fig. 13a) to 373 deg (Fig. 13d). This range of 13 deg corresponds to the passing duration of the vortex on the blade. From Figs. 13b–13d, the location of the vortex is clearly visible and corresponds to the circular pressure loss on the blade. A dotted circle representing the theoretical location of the vortex core has been added for visualization. In all the figures, the effect of the interaction on the pressure coefficient is mostly located at the blade leading edge, extending from blade tip to blade root, due to the slow decay of the vortex tangential velocity. In Fig. 13a, the vortex creates a pressure increase above the vortex center and a pressure decrease below, corresponding respectively to local negative and positive thrusts. This feature is also visible in the other figures but appears weakened. What we observe is in complete agreement with the variation of the relative upwash velocity, displayed in Fig. 12c, which indicates a positive upwash beneath the interaction radius (i.e., a pressure decrease at the leading edge on suction side) and a negative upwash above (i.e., a pressure increase at the leading edge on suction side). Accordingly, the variation of the pressure coefficient at the leading edge is also nonsymmetric with respect to the vortex core. Below the vortex core, the pressure decrease near the leading edge is higher in magnitude due to the stronger variation of the angle of attack and velocity upwash. It spreads on a larger span extent due to the location of the interaction at $R_i = 0.9R_i$, which is closer to the blade tip. Furthermore, in Fig. 13a, the radius along the blade span, which separates the positive and negative pressure areas, is located at $r \approx 0.93R_i$, which is very close to the radius of zero angle of attack

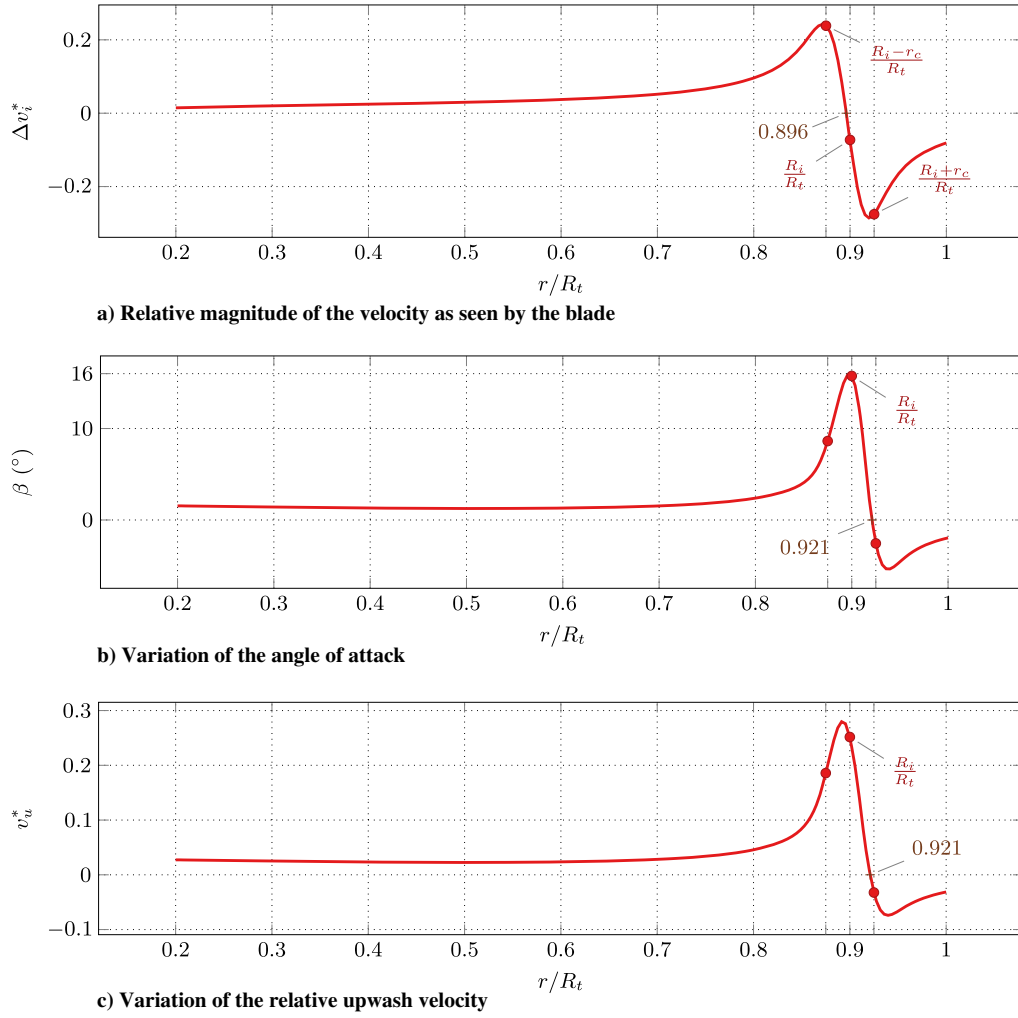


Fig. 12 Variations of the gust velocity as a function of the blade span, when the blade is at azimuth zero position, for the interaction with a Batchelor vortex.

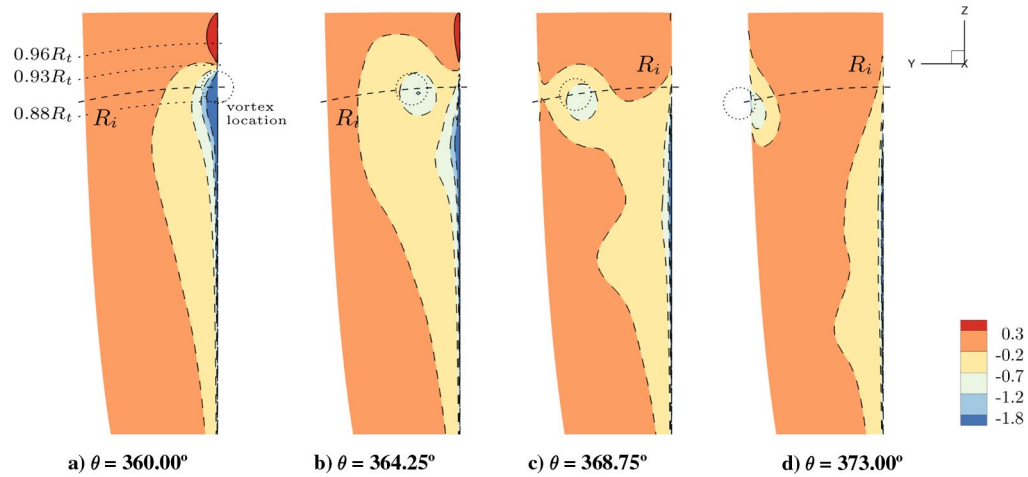


Fig. 13 Evolution of the pressure coefficient C_p on the blade suction side for four successive azimuths for the interaction with a Batchelor vortex.

and null upwash in Fig. 12c, at $r \approx 0.921R_t$. The minimum pressure on the leading edge is reached at radius $r \approx 0.88R_t$, and the pressure maximum at radius $r \approx 0.96R_t$, which is close to the values obtained for the maximal and minimal relative upwash velocities. These radii have been added in Fig. 13a as thin dashed arcs. If we limit the observation to the interaction radius arc during the passing of the vortex, we observe the same behavior as described by Doolan et al. [24]: a local suction on the blade, which follows the vortex and is of high amplitude on the blade leading edge. Figure 14 represents the

pressure coefficient along with the streamlines on the blade leading edge, when the blade is at azimuth 360 deg. The blade is displayed for $r \geq 0.8R_t$, and its thickness has been amplified by a factor of 10 for visualization purpose. The theoretical location of the vortex core has been added as a semitransparent cylinder. The variations of pressure coefficient we have observed on the suction side in Fig. 13a are clearly visible. This variation is of opposite sign on the pressure side. Beneath the interaction radius, the pressure fluctuation is of higher amplitude on the blade suction side than on the pressure side.

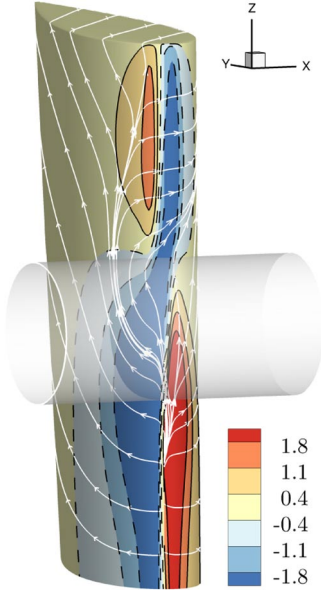


Fig. 14 Pressure coefficient C_p and streamlines on the blade leading edge at azimuth 360 deg for the interaction with a Batchelor vortex. Blade thickness has been exaggerated.

This trend is opposite above the interaction radius, which conforms to the observations of Ahmadi [2]. We observe a connection between the pressure loss areas on the two sides. The streamlines show the dissymmetry of the flow, due to the presence of the vortex. The vortex creates a local variation of the blade incidence, leading to an acceleration of the flow on the suction side and a deceleration on the pressure side beneath the vortex as well as a deceleration of the flow of the suction side and an acceleration on the pressure side above the vortex.

The noise radiated in the far field by the interaction has been computed using the blade pressure fluctuations for observation points located on a sphere. For each frequency, sound pressure level (SPL) and sound power level (SWL) will be used for the analysis.

The SWL (SWL_{dB} in dB) is computed for each frequency f as the integral of the SPL (SPL_{dB} in dB) recorded for each microphone on the surface S_{mic} :

$$SWL_{dB}(f) = 10 \log_{10} \int_{S_{mic}} 10^{SPL_{dB}(s,f)/10} ds \quad (17)$$

Figure 15 shows the distribution of SWL depending on the frequency expressed in terms of multiples of the blade-passing frequency (BPF). The maximal SWL value of 110.8 dB is reached for low frequencies, at $f = 2BPF$, and acoustic power decreases gradually above this point. The slope of the curve is nearly constant and the acoustic power decreases by about 2 dB every 10BPF.

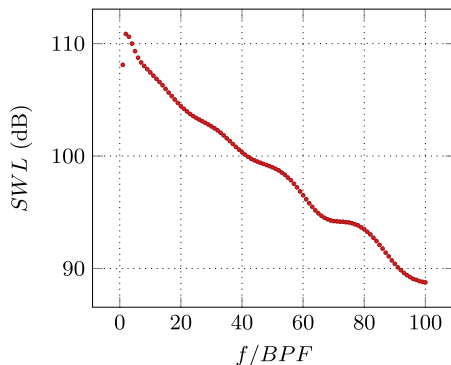


Fig. 15 Distribution of the SWL of the noise radiated for the interaction with a Batchelor vortex.

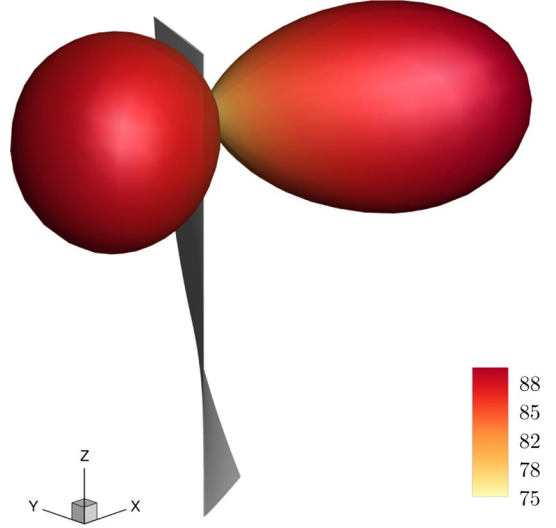


Fig. 16 OASPL far-field directivity pattern for the interaction with a Batchelor vortex, in decibels; blade at azimuth zero position.

The far-field directivity of the overall sound pressure level (OASPL), integrated over all frequencies, is displayed Fig. 16, together with the blade at azimuth zero position, added for visualization purpose. The shape is expressed in pascals squared and the color levels in decibels. The directivity pattern is dipolarlike, as observed in the studies of Schlinker and Amiet [1], Ahmadi [2], and Roger et al. [6], with a forward lobe smaller than the one directed backward and both lobes oriented obliquely toward the blade rotation direction. The extremities of both lobes, which correspond to the maximal OASPL values, are located in the (u_x, u_y) plane passing by the point $(0, 0, R_i)$. The front lobe extremity has an angle of 8.8 deg with the x axis and the rear lobe extremity an angle of 153.3 deg.

Figure 17 shows the far-field directivity patterns for different tones from the rotation fundamental ($f = BPF$), in Fig. 17a, to $f = 31BPF$, Fig. 17d, in pascals squared for the shape and in decibels for the color levels. Each figure has a different scale to be displayable, but they all share the same color levels. These directivity patterns are dipolarlike for the selected range of frequencies, with maximum levels oriented forward for very low frequencies and switching progressively to backward for higher frequencies. As expected from the SWL Fig. 15, the directivity for $f = BPF$ exhibits the largest levels among the other selected frequencies. Yet, the combination of tangential and axial velocities in the vortex model does not permit quantifying the contribution of each component on the radiated noise. To do so, separated computations considering the tangential and axial velocity fields only have been carried out and are presented hereafter.

B. Interaction with a Lamb–Oseen Vortex and a Gaussian Deficit

The contribution of the tangential velocity field on the interaction can be quantified by setting the axial velocity deficit to zero. The Batchelor vortex defined by Eqs. (2) and (3) reduces then to the Lamb–Oseen vortex [42–45], for which the pressure field under a homentropic assumption is given by Eq. (7). On the other hand, the contribution of the axial velocity field is obtained when the tangential velocity is null, and the flow disturbance interacting with the blade consists of a Gaussian axial velocity deficit. To observe and quantify the background noise due to the composite mesh, we have computed one extra case with no vortex, with the flow consisting only of the uniform upstream velocity.

For both the Lamb–Oseen and the Gaussian cases, the velocity profiles extracted from the steady simulations using the same process as for Fig. 9 are in good agreement with the flow injected at the inlet boundary. The largest differences occur for the axial velocity deficit in the core; for the Lamb–Oseen vortex, it is less than 1% of the initial Batchelor vortex value, and for the Gaussian velocity deficit, it is

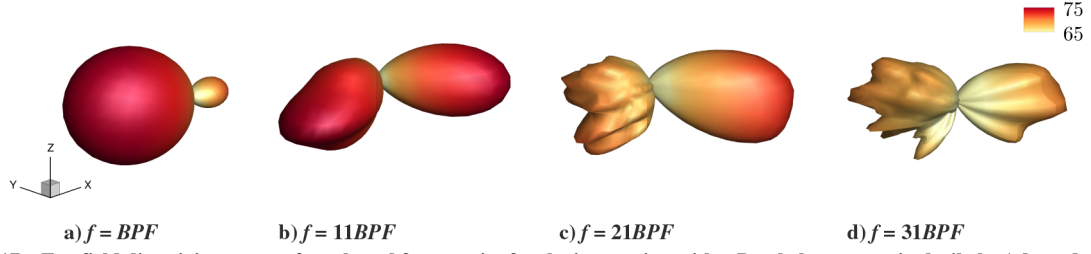


Fig. 17 Far-field directivity pattern for selected frequencies for the interaction with a Batchelor vortex, in decibels. Adapted scale.

3.2% lower. We conclude that the numerical setup is accurate enough to support these flows here as well.

The effect of the Lamb–Oseen vortex and the Gaussian velocity deficit on the velocity seen by the blade at azimuth zero is plotted in Fig. 18. Values corresponding to the interaction with a Batchelor vortex have been kept for comparison. The nondimensional relative magnitude, defined by Eq. (14), is displayed Fig. 18a. Few differences are observed between the Batchelor and the Lamb–Oseen cases, with slightly greater values in the vortex core. The new extremum values are 0.26 at lower core radius and -0.24 at upper core radius, which is close to the tangential velocity magnitude, set to $(1/4)v_h$. The position of zero relative magnitude corresponds to the vortex center, which makes sense because there is no velocity modification in the center of the vortex. We observe many more differences with the Gaussian deficit alone; because of the compactness of the contribution, most of the relative magnitude is

null, except inside the core, where it is negative and has a minimal value of -0.07 reached in the deficit center. We observe that the effect of the two contributions combine pretty well to obtain the curve corresponding to the Batchelor case. Especially in the core, the relative magnitude due to the tangential contribution is lowered by the negative relative magnitude of the axial contribution. We conclude that the relative magnitude variation is mostly due to the tangential component of the vortex.

Figure 18b displays the variation of the relative angle of attack, as defined by Eq. (15). We observe here as well that the tangential contribution has a wide influence, whereas the axial contribution is localized in the vortex core. For the Lamb–Oseen vortex, the angle of 0 deg is reached at the vortex center, and the extremum values are 5.2 deg at lower core radius and -7.8 deg at upper core radius. We also observe that the angle of attack sign change is due to the tangential component. For the Gaussian contribution, we observe a

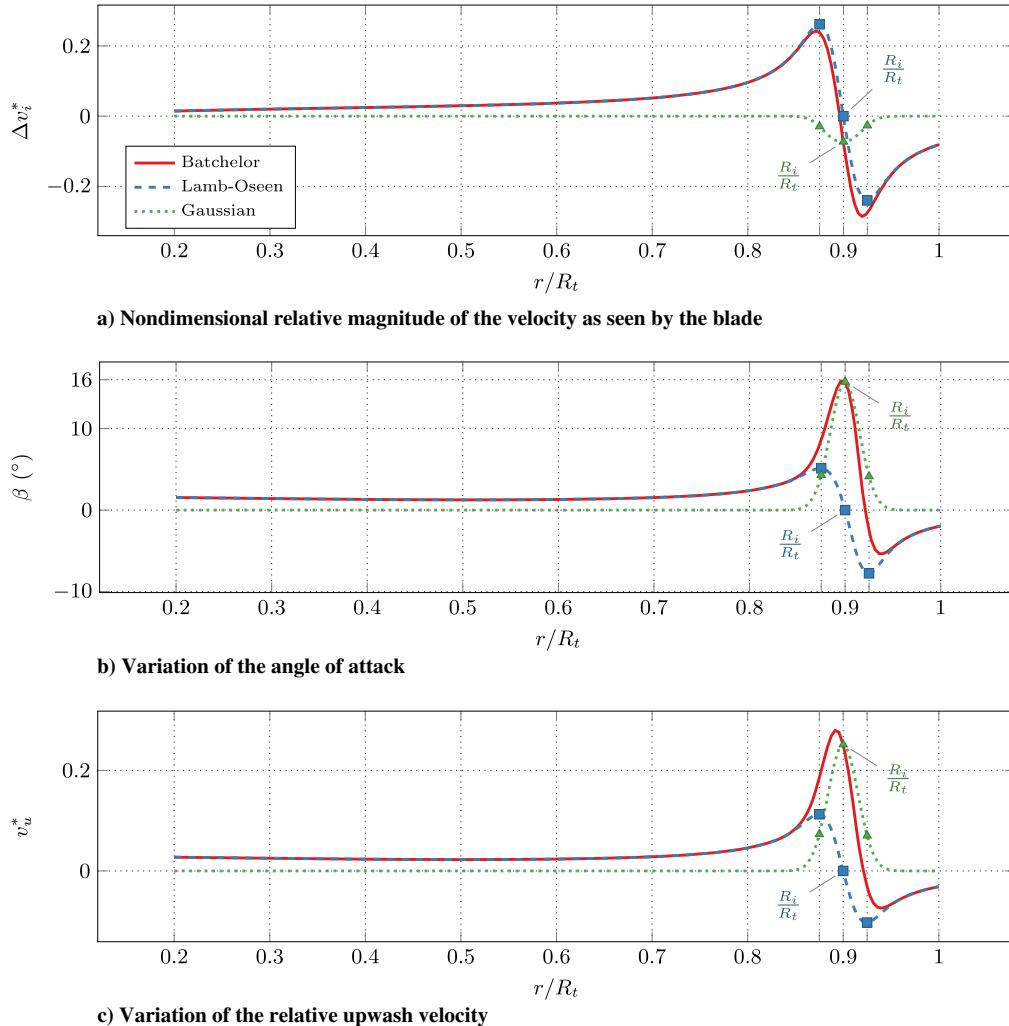


Fig. 18 Variations of the gust velocity as a function of the blade span, when the blade is at azimuth zero position, for the interaction with different flow disturbance models.

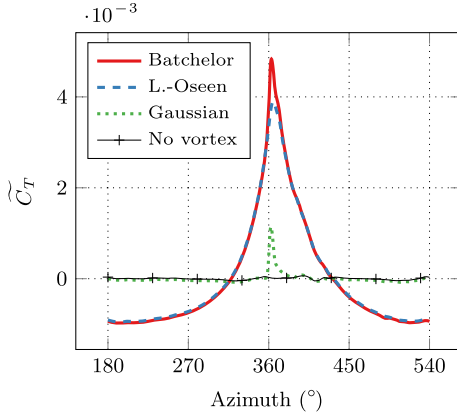


Fig. 19 Evolution of the fluctuation of the thrust coefficient as a function of the azimuthal angle for the interaction with different flow disturbance models.

Table 5 Comparison of the thrust coefficient average \bar{C}_T

Case	Thrust coefficient average
Batchelor	4.898×10^{-3}
Lamb-Oseen	4.87×10^{-3}
Gaussian	5.020×10^{-3}
No vortex	4.994×10^{-3}

pulse in the core of amplitude 15.7 deg. We conclude that the pulse of angle of attack observed in the Batchelor case is due to the axial component of the vortex velocity.

Figure 18c displays the variation of the dimensionless relative upwash velocity, defined by Eq. (16). The tangential component creates a positive upwash velocity beneath the interaction radius and negative above. Maximum amplitudes are reached very close to the vortex core radii, at $r \approx 0.874R_t$ for the maximum of 0.113 and at $r \approx 0.924R_t$ for the minimum of -0.103 . The axial velocity component creates a positive pulse of velocity centered around the vortex core radius, with an amplitude of 0.252. We conclude that the pulse of upwash velocity observed for the interaction with a Batchelor vortex is due to the axial velocity component, whereas its change of sign is due to the tangential velocity component.

Figure 19 displays the evolution of the fluctuating thrust coefficient \tilde{C}_T as a function of azimuth. Table 5 gives the different values of the mean thrust coefficient \bar{C}_T . The curves corresponding to the Lamb-Oseen vortex match very well with that of the Batchelor

vortex, except in the range from 355 to 380 deg, where the amplitude is lower for the Lamb-Oseen vortex. The maximum of thrust is reached for an azimuth of about 365 deg. On the other hand, for the Gaussian velocity deficit, the thrust pulse is sharper, due to the compactness of the velocity disturbance. The interaction with the blade is visible for azimuth close to 360 deg, with a maximum at 362 deg. Outside of this pulse, the thrust fluctuation is close to zero. We observe that the two contributions can combine to obtain the Batchelor curve. For the case without vortex, the thrust coefficient fluctuation is lower than 6.5×10^{-5} . Small fluctuations are observed by instance near azimuth 400 deg, which are present for the Gaussian deficit and thus correspond to artifacts due to the numerical setup.

Figure 20 displays the pressure coefficient C_p on the suction side of the blade and Fig. 21 the pressure coefficient along with flow streamlines on the leading edge, as in Fig. 14. For the Lamb-Oseen vortex, we observe in Fig. 20b a similar behavior as the interaction with a Batchelor vortex; the vortex creates a pressure increase above the interaction point and a pressure decrease below. The span location that separates the pressure variation areas is now located at $r \approx 0.91R_t$, which is lower compared to the Batchelor vortex case but is consistent with the location where the upwash velocity changes its sign in Fig. 18c, at $r = R_t$. The maximum pressure coefficient on the leading edge is located at radius $r \approx 0.95R_t$ and the minimum at radius $r \approx 0.86R_t$, which is close to the theoretical values. These radii are plotted as dashed arcs on the blade. We observe in Fig. 21b similar results as well.

For the Gaussian velocity deficit, however, we see in Fig. 20c that the behavior is different. The influence of the velocity deficit is clearly located at the interaction radius and results in a local suction corresponding to an increase of upwash velocity and the generation of a positive thrust. Figure 21c shows that the pressure variation is of opposite sign on the pressure side, which means that the axial velocity deficit puts the blade on incidence locally. We clearly observe here the dissymmetry caused by the axial velocity, as described by Liu and Marshall [20].

Figure 22 shows the distribution of SWL for the interaction with the Lamb-Oseen vortex and the Gaussian velocity deficit, along with the results obtained with the Batchelor vortex. For the interaction with a Lamb-Oseen vortex, the maximal value is reached for the frequency $f = 2\text{BPF}$ as for the Batchelor vortex. The maximum of 110.2 dB is very close to that obtained for the Batchelor case. Then, the acoustic power decreases gradually, but the decay between the BPF and 24BPF is much more pronounced for the Lamb-Oseen vortex interaction where the acoustic power decreases by about 7 dB every 10BPF. After this frequency of 24BPF, the slope decreases to 2 dB every 10BPF, similar to the Batchelor vortex case, and the two curves are separated by a nearly constant shift of 8 dB. On the other hand, the distribution of SWL resulting from the interaction with the Gaussian velocity deficit differs strongly. The SWL is very low for

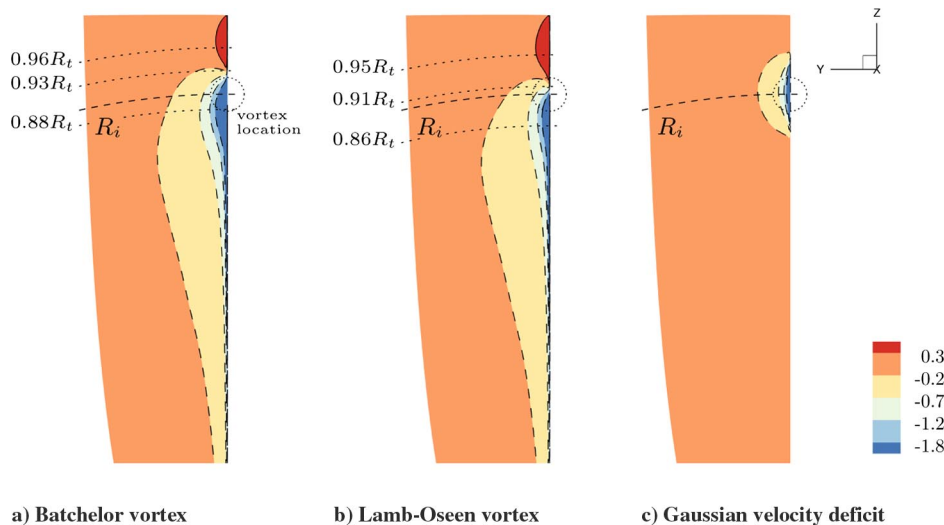


Fig. 20 Pressure coefficient C_p on the suction side of the blade for azimuth 360 deg for the interaction with different flow disturbance models.

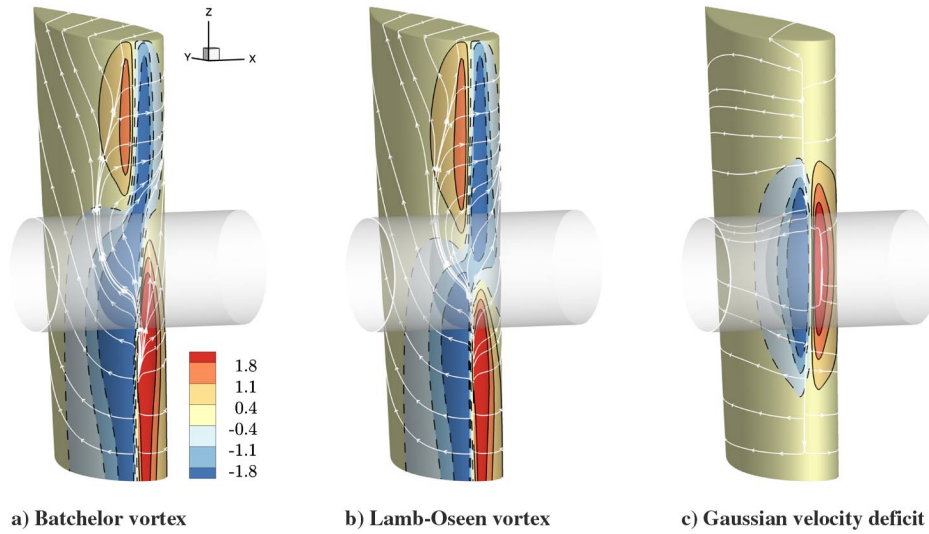


Fig. 21 Pressure coefficient C_p and streamlines on the blade leading edge at azimuth 360 deg for the interaction with different flow disturbance models. Blade thickness has been exaggerated.

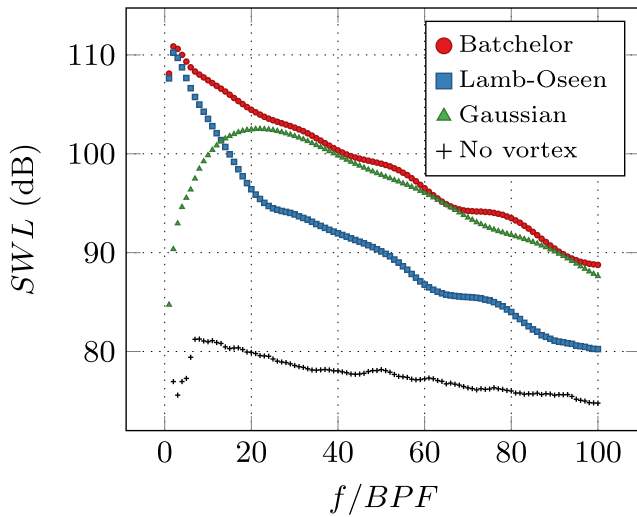


Fig. 22 Acoustic power for the interaction with different flow disturbance models.

frequencies close to the fundamental and increases strongly up to the maximum value of 102 dB, reached for about 21BPF. Beyond this point, the SWL decreases with the same values as the Batchelor vortex interaction and with the same slope of 2 dB every 10BPF. The frequency of maximum SWL is close to the change of slope in the decay rate observed for the Lamb–Oseen interaction case. Then, the SWL distribution resulting from the absence of vortex determines the noise due to the numerical setup. It has a peak of 81 dB reached at 7BPF, then it decreases with a rate of 0.6 dB every 10BPF. The SWL is nearly constant compared to the other interaction cases. It is observed that the SWL distribution of the other interaction cases is always between 5 and 20 dB above this one, which means that the numerical setup is accurate enough to not interfere with the results. We conclude that the noise generated by the tangential velocity dominates for low frequencies, whereas the noise generated by the axial velocity dominates for high frequencies. The transition between the two frequency ranges is located at $f \approx 13$ BPF. Moreover, the low-frequency harmonics have higher amplitude compared to the high-frequency ones, by about 10 dB.

The far-field directivity of the OASPL for both interactions is displayed Fig. 23. For the Lamb–Oseen case, the result is very close in terms of shape to the one obtained for the Batchelor vortex case. The shape is dipolarlike, but with lower values of maximum radiated

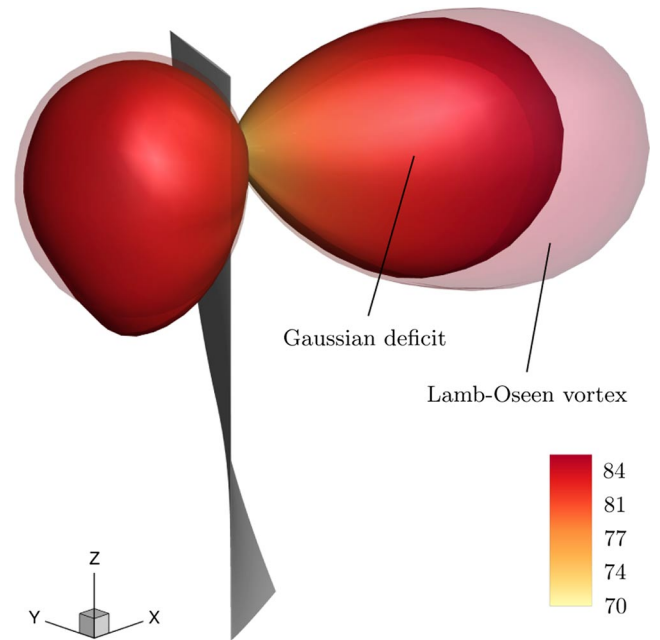


Fig. 23 OASPL far-field directivity pattern for the interaction with a Lamb–Oseen vortex and a Gaussian velocity deficit, in decibels; blade at azimuth zero position.

noise. For the Gaussian case, the shape is dipolarlike as well, which is in agreement with the pressure fluctuation observed on the blade in Fig. 20c. The amplitude of the lobes is close to the Lamb–Oseen interaction case, but with a smaller rear lobe. Like for the two previous cases, the two lobes are oriented obliquely in the blade rotation direction. It is interesting to note that the interaction with a Lamb–Oseen vortex has higher radiated noise levels compared to the interaction with a Gaussian velocity deficit, whereas its upwash velocity is lower, as observed in Fig. 18c. As we have pointed out, the tangential contribution is low in amplitude but spreads along the entire blade span. On the contrary, the axial contribution is high in amplitude but remains limited to the interaction location. Because the low-frequency harmonics have higher SWL compared to the high-frequency ones, the directivity pattern mainly reflects the tendency of the low frequencies.

The far-field directivity patterns for different tones are displayed in Figs. 24 and 25. For the Lamb–Oseen vortex case, in Fig. 24, contrary to the Batchelor vortex, we observe a transition from a

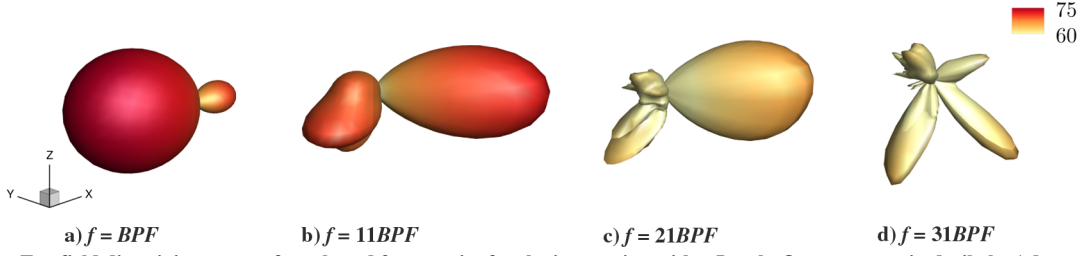


Fig. 24 Far-field directivity pattern for selected frequencies for the interaction with a Lamb–Oseen vortex, in decibels. Adapted scale.

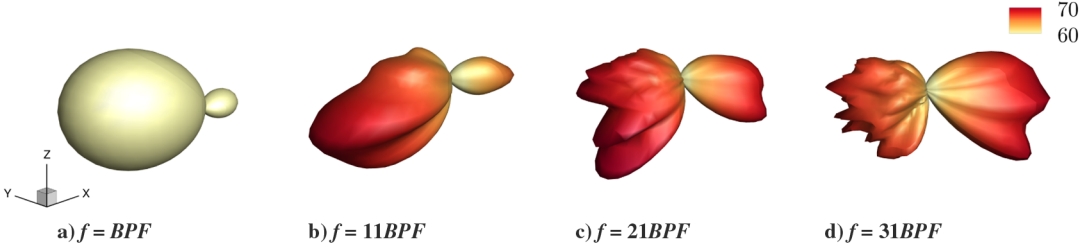


Fig. 25 Far-field directivity pattern for selected frequencies for the interaction with a Gaussian velocity deficit, in decibels. Adapted scale.

dipolarlike to a quadrupolarlike directivity. The analysis of the directivity patterns for the other harmonic frequencies reveals that this transition occurs around 27BPF. The frequency at which the transition occurs is directly linked to the distance between the blade tip and the location of interaction with the vortex center. In the present case, for frequencies higher than 27BPF, the pressure fluctuations on the blade produce two dipoles pulsating with opposite phases and located on both sides of the interaction radius (i.e., at $r = R_i + r_c$ and $r = R_i - r_c$). The resulting directivity of these two dipolar sources is thus very close to a unique quadrupole source that would be located at $r = R_i$. For frequencies lower than 27BPF, the noise radiation results mostly from the inner part of the blade where the pressure fluctuations have the same sign and phase along the span, resulting in classical dipolarlike patterns. This transition between quadrupolar and dipolar directivity pattern is in good agreement with the model of Roger et al. [7]. Figure 25 shows the far-field directivities for the interaction with a Gaussian velocity deficit. For the entire range, the pattern has a dipolar shape, as opposed to the Lamb–Oseen case. As expected from the analysis of the SWL plotted in Fig. 22, the frequency $f = 21\text{BPF}$ corresponds to the most powerful tone of the interaction. As for the Lamb–Oseen case, this dipolar contribution is part of the Batchelor vortex interaction. Because its acoustic power is far larger than the Lamb–Oseen contribution for frequencies higher than 21BPF, the quadrupolarlike radiation resulting from the tangential velocity field is overwhelmed by the dipolarlike radiation.

C. Analysis of the Coupling Effect Between the Velocity Components

The preceding section, addressing the interactions of the blade with an azimuthal velocity disturbance only (Lamb–Oseen vortex) and with an axial velocity disturbance only (Gaussian velocity deficit), has proven that the noise radiated by the orthogonal BVI with a Batchelor vortex is strongly linked to the azimuthal velocity field for frequencies close to the BPF and strongly linked to the axial velocity field for higher frequencies. For the frequency range in between, Fig. 22 shows that the SWL radiated by the interaction with a Batchelor vortex is much higher than the SWL radiated by the interaction with a Lamb–Oseen vortex and a Gaussian velocity deficit. A rational hypothesis is that, for this frequency range, the acoustic waves radiated by the interaction with a Batchelor vortex equal the sum of the acoustic waves radiated separately by the interaction with its components.

We have calculated a reconstructed fluctuating pressure based on the coherent sum of the pressure on the blade for the interaction

with the separated components of the Batchelor vortex: $p_f = p_{LO} + p_G - \bar{p}_{LO} - \bar{p}_G$, where p_{LO} and \bar{p}_{LO} are the instantaneous and mean pressures for the interaction with a Lamb–Oseen vortex, and p_G and \bar{p}_G are the instantaneous and mean pressures for the interaction with a Gaussian velocity deficit. As for the previous cases, the noise radiated by this new fluctuating pressure on the blade has been computed using the solid surface formulation of the Ffowcs Williams and Hawkings equation. On the other hand, we have also summed the SWL radiated separately by the interaction with a Lamb–Oseen vortex and a Gaussian velocity deficit, leading to a noncoherent sum.

The SWLs radiated by these coherent and noncoherent sums are plotted in Fig. 26, together with the SWLs radiated by the interaction with a Batchelor vortex, a Lamb–Oseen vortex, and a Gaussian velocity deficit.

If the blade response to the tangential and axial velocity disturbances were uncorrelated, the SWLs of both coherent and noncoherent sums would be identical to the SWL of the Batchelor case. What we observe is that the levels for the coherent sum match exactly the levels for the Batchelor case in the frequency range

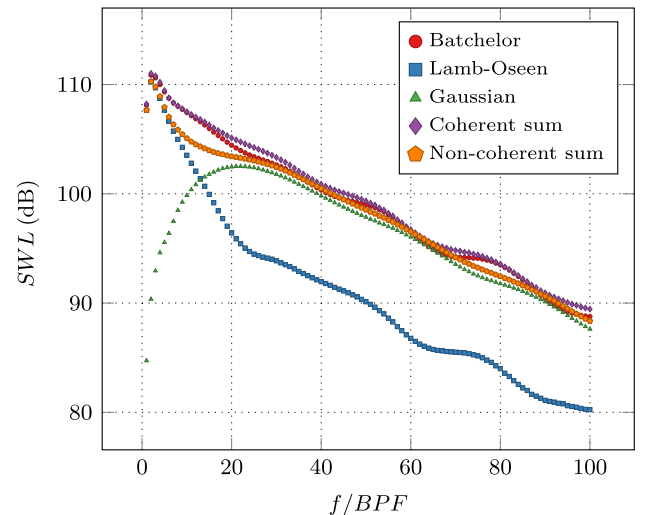


Fig. 26 Reposition of the SWL radiated by the blade as a function of multiples of the BPF for the interaction with a Batchelor vortex from its separated components.

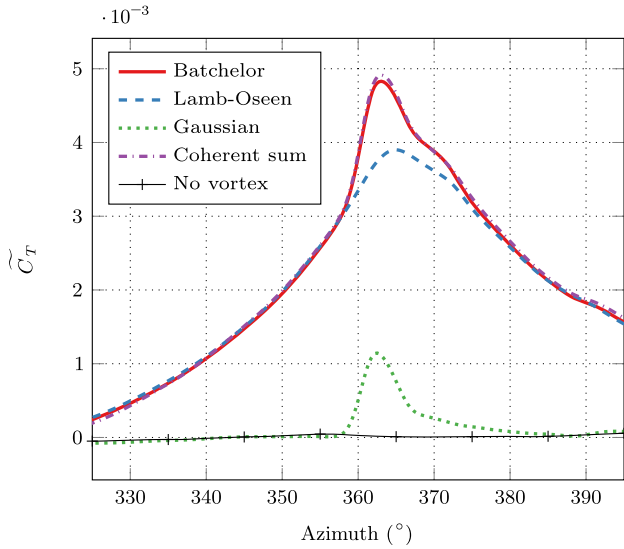


Fig. 27 Recomposition of the thrust coefficient for the interaction with a Batchelor vortex from its separated components. Detail on azimuth close to 360 deg.

between 2 and 21BPF, whereas the levels of the noncoherent sum underestimate significantly the radiated noise in this frequency range. This difference highlights a phenomenon of constructive interferences between the two velocity contributions, which cannot be taken into account by a noncoherent sum. Above 21BPF, the levels of both sums are very close to the levels of the Batchelor case, with a maximum error in both cases lower than 1 dB. They decrease by about 2 dB every 10BPF. The SWL of the coherent sum is for most of the frequencies a bit higher than the SWL of the Batchelor case.

The interpretation of constructive interferences between the velocity components of the Batchelor vortex makes sense only if the recombination of the individual contributions admits a principle of superposition. It is well known that the Ffowcs Williams and Hawkings operator is linear, whereas the Euler equation is nonlinear. Consequently, we have to verify if this linearity appears in the CFD results.

Figure 27 displays variations of the fluctuating thrust coefficient obtained in Secs. IV.A and IV.B. It shows the sum of the thrust fluctuation coefficients obtained before. The range of azimuths has been restrained close to azimuth 360 deg where the interaction occurs. We see that both curves are almost the same. The amplitude of the sum for its maximal value is 1.66% higher than the amplitude obtained for the Batchelor vortex interaction. The small differences have several origins. As observed in the figure and in Fig. 19, the computational setup used generates a small parasite thrust fluctuation when there is no vortex to interact with the blade. This parasite thrust is doubled during the recombination process. Moreover, the thrust superposition does not reproduce flow nonlinearities. We conclude that the contribution of the two velocity components is linear in the CFD results.

Figure 28 shows the OASPL directivity pattern. The Batchelor vortex pattern has been kept for comparison. The two patterns have similar behavior; they have the same dipolar shape, and the lobes have the same orientation. The sum has, however, a slightly larger amplitude, which coincides with the overall higher SWL of this case observed in Fig. 26.

The far-field directivity patterns from the sum is plotted Fig. 29 for different frequencies. The shapes are very close to the Batchelor case shown in Fig. 17.

The constructive contribution to the radiated noise due to the tangential and axial velocities is clearly observed in the acoustic signatures. The acoustic signatures computed for the probe with the highest OASPLs are plotted for the front probe in Fig. 30a and for the rear probe in Fig. 30b. The two signals are similar with opposite

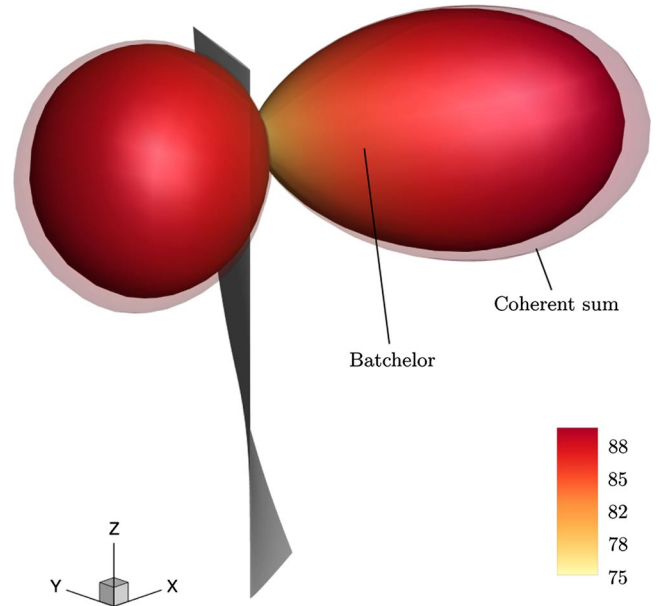


Fig. 28 OASPL far-field directivity pattern for the interaction with a Batchelor vortex and the coherent sum of its components, in decibels; blade at azimuth zero position.

signs. The contribution of each velocity components is clearly visible; the signature of the Lamb–Oseen case has a wide spread, whereas the signature of the Gaussian case is more compact. For each probe, there is a first pressure pulse followed by a second one of the opposite sign and lower amplitude. The tangential and axial velocity component signatures add their contributions in a constructive way that matches the amplitude of the Batchelor case. The signatures of the sum, added to the plot, are in really good agreement with the signature of the Batchelor vortex interaction. The signature of the pressure radiated without any vortex is added to the picture. For both probes, it has a very low level that does not interfere with the other observations.

We conclude that a phenomenon of constructive interferences exists between the two velocity components in the frequency range between 2 and 21BPF. This is permitted by the fact the two contributions are linearly superposed. The sum of the pressure fluctuations on the blade from a Lamb–Oseen case and a Gaussian case is very close to the pressure fluctuations on the blade from a complete Batchelor case. Thus, the acoustic directivities and sound power levels of this reconstructed case are similar with a Batchelor case.

D. Variation of the Swirl Number

The previous computations considered a Batchelor vortex and its separated components for a swirl number $q = 1$. We can wonder how the value of the swirl number will affect the main results of the previous sections and whether the superposition principle will remain true. Consequently, we have computed interaction cases for Batchelor vortices with swirl numbers $q = 2$ and $q = 0.85$. To this aim, we have kept the tangential velocity amplitude constant and made the axial velocity amplitude vary. We have also investigated the relative influence of the velocity components for these cases, which leads to a total of six computations.

The thrust coefficient fluctuation is plotted in Fig. 31. Previous values from the Batchelor vortex with $q = 1$ have been kept as reference for the comparison. Figure 31a displays the fluctuating thrust for $q = 2$, and Fig. 31b displays the results for $q = 0.85$. The difference between the two figures is due to the axial velocity component, which decreases when the swirl number increases. The thrust fluctuation for the sum, obtained as in Sec. IV.C by adding the axial and tangential contributions, matches the Batchelor curve very well in both cases.

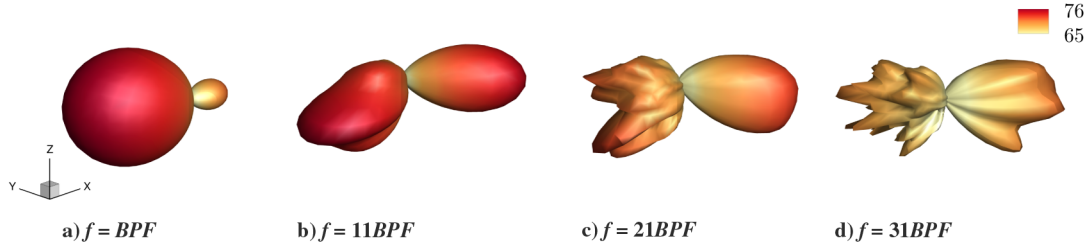


Fig. 29 Far-field directivity pattern for selected frequencies for the recomposition of the interaction with a Batchelor vortex, in decibels. Adapted scale.

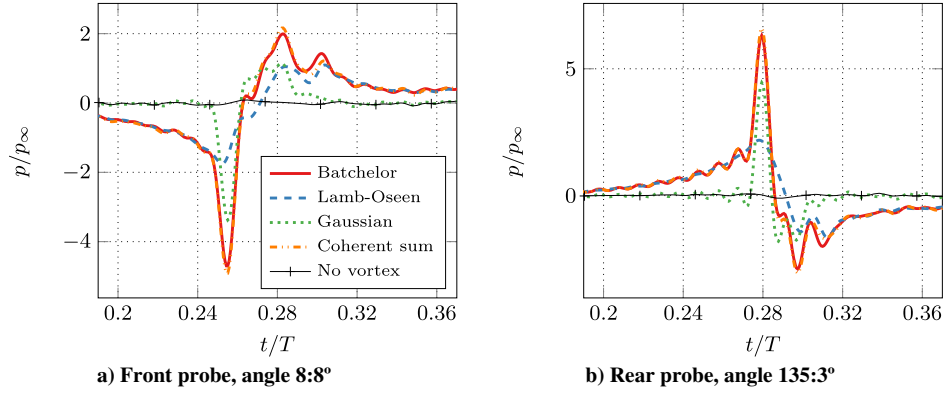


Fig. 30 Acoustic signatures of the interaction with different velocity disturbance models for the front and rear probes, which correspond to the highest acoustic pressure amplitudes.

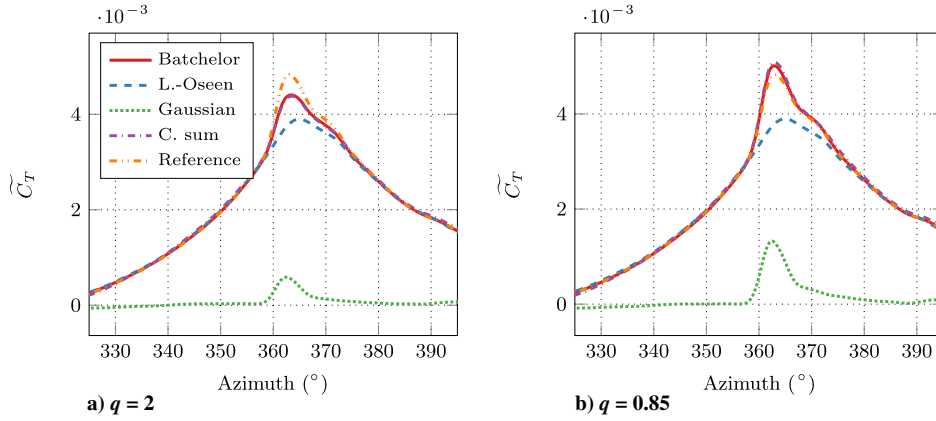


Fig. 31 Evolution of the thrust coefficient as a function of the azimuthal angle for different swirl numbers for the interaction with a Batchelor vortex and its velocity components.

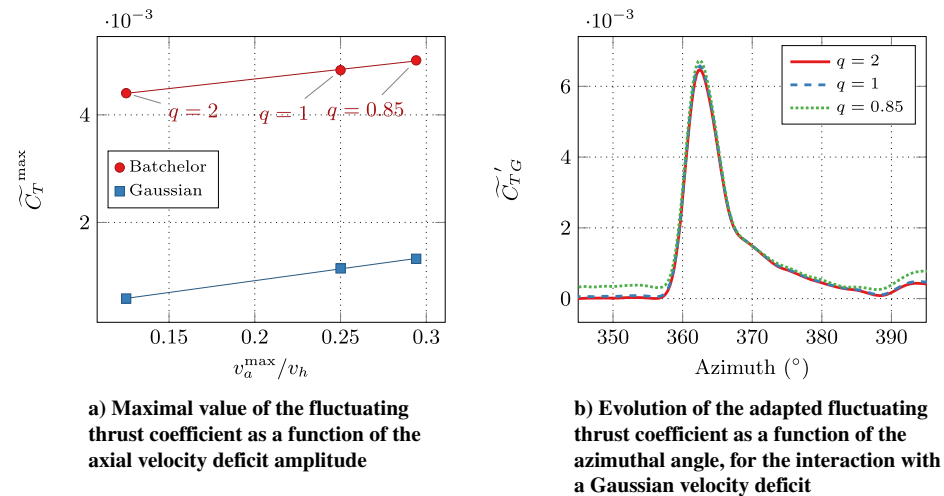


Fig. 32 Linear correlation between the thrust coefficient and the axial velocity deficit.

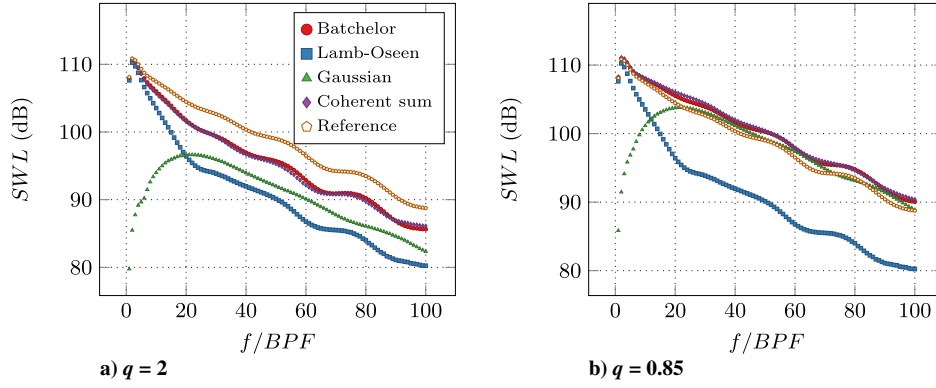


Fig. 33 Acoustic power of the SPLs radiated by the blade as a function of multiples of the BPF for different swirl numbers for the interaction with a Batchelor vortex and its velocity components.

Liu and Marshall [20] have observed a linear correlation between the thrust forces on the blade and the axial velocity deficit in the vortex. Their study involves a fixed rectilinear blade and a columnar vortex advected by the flow. Figure 32a displays the maximal value of the fluctuating thrust coefficient \bar{C}_T^{\max} as a function of the axial velocity deficit amplitude, for the interaction with a Batchelor vortex and a Gaussian velocity deficit. The tangential velocity amplitude is constant for the interactions, and only the axial velocity deficit amplitude varies, and so it is natural to observe a common variation of the maximum for both interactions. The value increases linearly with the axial velocity deficit amplitude, as observed by Liu and Marshall. The growth rate is of the same order of magnitude in both cases. Liu and Marshall have defined an adapted thrust coefficient, which is independent from the axial velocity deficit amplitude. For our case, we define this adapted thrust coefficient as the ratio between the fluctuation of the thrust coefficient and the dimensionless axial velocity deficit amplitude: $\bar{C}_T' = \bar{C}_T v_h / v_a^{\max}$. We have observed in Sec. IV.C that the thrust for the interaction with a Batchelor vortex is the addition of the thrusts for the Lamb–Oseen (\bar{C}_{TLO}) and Gaussian velocity deficit (\bar{C}_{TG}) velocity components (i.e., $\bar{C}_T = \bar{C}_{TLO} + \bar{C}_{TG}$). Because the Lamb–Oseen contribution is constant, the adapted thrust coefficient computed for the Gaussian contribution is displayed in Fig. 32b. The adapted values are in really good agreement when the interaction occurs, as observed by Liu and Marshall [20]. We conclude that the thrust due to the axial velocity deficit is proportional to the axial amplitude.

The SWL of these interactions is plotted in Fig. 33a for the case $q = 2$ and in Fig. 33b for the case $q = 0.85$. The modification of the amplitude of the axial velocity deficit results in a uniform increase or decrease of its corresponding SWL, which does not change the predominant frequency ranges of each velocity components. The behavior of the SWL remains driven by the axial velocity deficit above $f = 20$ BPF, but this behavior is weaker with high values of the swirl number. As in Sec. IV.C, we have built a pressure sum case with pressure values on the blade for the Lamb–Oseen case and for the Gaussian deficit case. The rebuilt curves for each value of q are in really good agreement with the Batchelor SWL curve.

These computations based on the variation of the axial velocity show that the mechanism of the interaction remains the same. This observation clears up any possible doubt with regard to the small numerical inaccuracy for the amplitude of the vortex axial velocity seen by the blade and discussed in the light of Fig. 9.

We conclude that the variation of the swirl number in the range investigated does not change the frequency range for each component: low frequencies are associated with the tangential velocity component, and high frequency (above $f = 21$ BPF) are associated with the axial velocity component. The intermediate frequency range in between also remains the same. We have observed that this variation does not interfere with the way that the separated tangential and axial velocity components combine to obtain the original Batchelor vortex main results. This confirms the linear superposition of the velocity components of the Batchelor vortex observed in the previous section.

V. Conclusions

This paper presents the aeroacoustic analysis of the orthogonal interaction between a rotating blade and a stationary vortex. The study relies on a numerical experiment involving a simplified nonlifting blade interacting with a homentropic Batchelor vortex. Values of the vortex core radius and tangential and axial deficit velocities have been chosen from previous studies. The simulations rely on the three-dimensional compressible Euler equations for the aerodynamic model and on the Ffowkes Williams and Hawkings integral method for the aeroacoustic calculation. The computational domain consists of a near-body curvilinear mesh, an off-body octree of Cartesian meshes, and a network of microphones in the far-field for the acoustic analysis.

Computations have been carried out for three different values of the swirl number, and for each case, the interaction with the complete vortex, its tangential velocity field only, and its axial velocity field only have been computed separately. In all cases, the interactions produce an increase of the thrust coefficient when the blade cuts the vortex and generate an unsteady pressure on the blade that results in the propagation of acoustic waves. The study has shown that the vortex tangential velocity component is responsible for the noise level at low frequencies, whereas the vortex axial velocity component is responsible for the noise level at high frequencies. The noise generated for the frequencies in between is due to the constructive addition of the noise generated separately by the interaction with each of the velocity components. The noise radiated in the far field by the interaction with a Batchelor vortex or with an axial velocity deficit has a dipolar directivity pattern for all frequencies. In the case of the interaction with a tangential velocity field only, there is a transition at about 27 BPF from dipolar to quadripolarlike directivity pattern. For all swirl numbers computed, we have observed that the blade aerodynamic response was linear and that the superposition principle can be applied to obtain the response for the Batchelor vortex interaction from the separate aerodynamic response of the interactions with the vortex tangential or axial velocity fields only.

This study focused on the influence of the vortex parameters only. Other parameters will be investigated in the future to better understand and reduce the orthogonal blade/vortex interaction noise, such as the location of the interaction radius on the blade span, the angle between the vortex axis and the blade, or the blade shape (thickness, sweep, camber).

Acknowledgment

P. Zehner would like to thank Y. Delrieux (Aerodynamics, Aeroelasticity and Acoustics Department, ONERA) for his advice, reviews, and support.

References

- [1] Schlinker, R. H., and Amiet, R. K., “Rotor-Vortex Interaction Noise,” *8th Aeroacoustics Conference*, April 1983. doi:10.2514/6.1983-720

- [2] Ahmadi, A. R., "An Experimental Investigation of Blade-Vortex Interaction at Normal Incidence," *Journal of Aircraft*, Vol. 23, No. 1, 1986, pp. 47–55.
doi:10.2514/3.45265
- [3] Cary, C. M., "An Experimental Investigation of the Chopping of Helicopter Main Rotor Tip Vortices by the Tail Rotor, Part 2: High Speed Photographic Study," NASA TR 177457, 1987.
- [4] Howe, M. S., "Contributions to the Theory of Sound Production by Vortex-Airfoil Interaction, with Application to Vortices with Finite Axial Velocity Defect," *Proceedings of the Royal Society of London A: Mathematical, Physical and Engineering Sciences*, Vol. 420, No. 1858, Nov. 1988, pp. 157–182.
doi:10.1098/rspa.1988.0122
- [5] Howe, M. S., "On Unsteady Surface Forces, and Sound Produced by the Normal Chopping of a Rectilinear Vortex," *Journal of Fluid Mechanics*, Vol. 206, Sept. 1989, pp. 131–153.
doi:10.1017/S0022112089002259
- [6] Roger, M., Schram, C., and Moreau, S., "On Open-Rotor Blade-Vortex Interaction Noise," *18th AIAA/CEAS Aeroacoustics Conference*, AIAA Paper 2012-2216, June 2012.
- [7] Roger, M., Schram, C., and Moreau, S., "On Vortex-Airfoil Interaction Noise Including Span-End Effects, with Application to Open-Rotor Aeroacoustics," *Journal of Sound and Vibration*, Vol. 333, No. 1, 2014, pp. 283–306.
doi:10.1016/j.jsv.2013.09.012
- [8] Quaglia, M. E., Moreau, S., Roger, M., and Fernando, R., "A 3D Analytical Approach for Open-Rotor Blade Vortex Interaction (BVI) Tonal Noise," *21st AIAA/CEAS Aeroacoustics Conference*, AIAA Paper 2015-2984, June 2015.
- [9] Quaglia, M. E., Léonard, T., Moreau, S., and Roger, M., "A 3D Analytical Model for Orthogonal Blade-Vortex Interaction Noise," *Journal of Sound and Vibration*, Vol. 399, July 2017, pp. 104–123.
doi:10.1016/j.jsv.2017.03.023
- [10] Amiet, R. K., "Airfoil Gust Response and the Sound Produced by Airfoil-Vortex Interaction," *Journal of Sound and Vibration*, Vol. 107, No. 3, 1986, pp. 487–506.
doi:10.1016/S0022-460X(86)80120-1
- [11] Vion, L., "Modification des Tourbillons d'Extrémité d'Hélices Contra-Rotatives en Vue d'Une Réduction des Nuisances Sonores," Ph.D. Thesis, École Polytechnique, Paris, April 2013.
- [12] Delattre, G., and Falissard, F., "Influence of Torque Ratio on Counter-Rotating Open-Rotor Interaction Noise," *20th AIAA/CEAS Aeroacoustics Conference*, AIAA Paper 2014-2969, June 2014.
- [13] Falissard, F., and Delattre, G., "Investigation of Counter Rotating Open Rotor Orthogonal Blade/Vortex Interaction Noise," *20th AIAA/CEAS Aeroacoustics Conference*, AIAA Paper 2014-2748, June 2014.
- [14] Coton, F., Marshall, J., Galbraith, R., and Green, R., "Helicopter Tail Rotor Orthogonal Blade Vortex Interaction," *Progress in Aerospace Sciences*, Vol. 40, No. 7, Oct. 2004, pp. 453–486.
doi:10.1016/j.paerosci.2004.11.001
- [15] Marshall, J. S., "Vortex Cutting by a Blade, Part I: General Theory and a Simple Solution," *AIAA Journal*, Vol. 32, No. 6, 1994, pp. 1145–1150.
doi:10.2514/3.12113
- [16] Marshall, J. S., and Yamamanchili, R., "Vortex Cutting by a Blade, Part II: Computation of Vortex Response," *AIAA Journal*, Vol. 32, No. 7, 1994, pp. 1428–1436.
doi:10.2514/3.12212
- [17] Marshall, J. S., and Grant, J. R., "Penetration of a Blade into a Vortex Core: Vorticity Response and Unsteady Blade Forces," *Journal of Fluid Mechanics*, Vol. 306, Jan. 1996, pp. 83–109.
doi:10.1017/S0022112096001243
- [18] Marshall, J. S., and Krishnamoorthy, S., "On the Instantaneous Cutting of a Columnar Vortex with Non-Zero Axial Flow," *Journal of Fluid Mechanics*, Vol. 351, 1997, pp. 41–74.
doi:10.1017/S0022112097007064
- [19] Krishnamoorthy, S., and Marshall, J. S., "Three-Dimensional Blade-Vortex Interaction on the Strong Vortex Regime," *Physics of Fluids*, Vol. 10, No. 11, 1998, pp. 2828–2845.
doi:10.1063/1.869805
- [20] Liu, X., and Marshall, J. S., "Blade Penetration into a Vortex Core with and Without Axial Core Flow," *Journal of Fluid Mechanics*, Vol. 519, Nov. 2004, pp. 81–103.
doi:10.1017/S0022112004001302
- [21] Filippone, A., and Afgan, I., "Orthogonal Blade-Vortex Interaction on a Helicopter Tail Rotor," *AIAA Journal*, Vol. 46, No. 6, 2008, pp. 1476–1489.
doi:10.2514/1.32690
- [22] Yildirim, E., and Hillier, R., "Numerical Modelling of the Impulsive Orthogonal Cutting of a Trailing Vortex," *Shock Waves*, Vol. 23, No. 4, July 2013, pp. 369–379.
doi:10.1007/s00193-012-0427-2
- [23] Doolan, C. J., Coton, F. N., and Galbraith, R. A. M., "Three-Dimensional Vortex Interactions with a Stationary Blade," *Aeronautical Journal*, Vol. 103, No. 1030, 1999, pp. 579–588.
doi:10.1017/S0001924000064216
- [24] Doolan, C. J., Coton, F. N., and Galbraith, R. A. M., "Surface Pressure Measurements of the Orthogonal Vortex Interaction," *AIAA Journal*, Vol. 39, No. 1, 2001, pp. 88–95.
doi:10.2514/2.1274
- [25] Doolan, C. J., Coton, F. N., and Galbraith, R. A. M., "The Effect of a Preceding Blade on the Orthogonal Vortex Interaction," *Journal of the American Helicopter Society*, Vol. 46, No. 3, 2001, pp. 221–227.
doi:10.4050/JAHS.46.221
- [26] Zehner, P., Falissard, F., and Gloerfelt, X., "A Numerical Experiment for the Aeroacoustic Study of Orthogonal Blade/Vortex Interaction," *Proceedings of the 22nd Congrès Français de Mécanique*, Association Française de Mécanique (AFM), 2015, pp. 1–6, <http://hdl.handle.net/2042/57709>.
- [27] Falissard, F., Zehner, P., Roger, M., and Gloerfelt, X., "Numerical and Analytical Investigation of Orthogonal Blade/Vortex Interaction Noise," *21st AIAA/CEAS Aeroacoustics Conference*, AIAA Paper 2015-2843, June 2015.
- [28] Zehner, P., Falissard, F., and Gloerfelt, X., "Aeroacoustic Study of the Interaction of a Rotating Blade with a Batchelor Vortex," *22nd AIAA/CEAS Aeroacoustics Conference*, AIAA Paper 2016-2999, June 2016.
- [29] Batchelor, G. K., "Axial Flow in Trailing Line Vortices," *Journal of Fluid Mechanics*, Vol. 20, No. 4, 1964, pp. 645–658.
doi:10.1017/S0022112064001446
- [30] Olendrar, C., Sellier, A., Rossi, M., and Huerre, P., "Inviscid Instability of the Batchelor Vortex: Absolute-Convective Transition and Spatial Branches," *Physics of Fluids*, Vol. 11, No. 7, July 1999, pp. 1805–1820.
doi:10.1063/1.870045
- [31] Colonius, T., Lele, S. K., and Moin, P., "The Scattering of Sound Waves by a Vortex: Numerical Simulations and Analytical Solutions," *Journal of Fluid Mechanics*, Vol. 260, Feb. 1994, pp. 271–298.
doi:10.1017/S0022112094003514
- [32] Delattre, G., Falissard, F., Vion, L., and Jacquin, L., "Open Rotor Interaction Noise Reduction Through Front Rotor Wake Modification," *International Journal of Aeroacoustics*, Vol. 15, Nos. 1–2, March 2016, pp. 207–227.
doi:10.1177/1475472X16643461
- [33] Gardarein, P., "Calculs Aérodynamiques des Hélices Rapides Transsoniques," ONERA—The French Aerospace Lab. TP 1991-218, Palaiseau, France, 1991.
- [34] Benoit, C., Péron, S., and Landier, S., "Cassiopee: A CFD Pre- and Post-Processing Tool," *Aerospace Science and Technology*, Vol. 45, Sept. 2015, pp. 272–283.
doi:10.1016/j.ast.2015.05.023
- [35] Péron, S., and Benoit, C., "Automatic Off-Body Overset Adaptive Cartesian Mesh Method Based on an Octree Approach," *Journal of Computational Physics*, Vol. 232, No. 1, 2013, pp. 153–173.
doi:10.1016/j.jcp.2012.07.029
- [36] Steger, J., Dougherty, F., and Benek, J., "A Chimera Grid Scheme," *Advances in Grid Generation*, edited by K. N. Ghia, and U. Chia, *ASME FED*, Vol. 5, American Soc. of Mechanical Engineers (ASME), Fluid Engineering Div. (FED), New York, 1983, pp. 59–69.
- [37] Benoit, C., Jeanfaivre, G., and Canonne, E., "Synthesis of ONERA Chimera Method Developed in the Frame of CHANCE Program," *Proceedings of the 31st European Rotorcraft Forum*, European Rotorcraft Forum (ERF), Sept. 2005, pp. 1–8, <http://hdl.handle.net/20.500.11881/1251>.
- [38] Saunier, O., Péron, S., Jeanfaivre, G., Benoit, C., and Lerat, A., "High-Order Accurate Cartesian Partitioning Methods. Application to Rotor Flows," *Proceedings of the 33rd European Rotorcraft Forum*, European Rotorcraft Forum (ERF), Sept. 2007, pp. 1–16, <http://hdl.handle.net/20.500.11881/216>.
- [39] Saunier, O., Benoit, C., Jeanfaivre, G., and Lerat, A., "Third-Order Cartesian Overset Mesh Adaptation Method for Solving Steady Compressible Flows," *International Journal for Numerical Methods in Fluids*, Vol. 57, No. 7, 2008, pp. 811–838.
doi:10.1002/(ISSN)1097-0363
- [40] Ffowes Williams, J. E., and Hawkings, D. L., "Sound Generation by Turbulence and Surfaces in Arbitrary Motion," *Philosophical Transactions of the Royal Society*, Vol. 264, No. 1151, 1969, pp. 321–342.
doi:10.1098/rsta.1969.0031
- [41] Prieur, J., and Rahier, G., "Aeroacoustic Integral Methods, Formulation and Efficient Numerical Implementation," *Aerospace Science and*

- Technology*, Vol. 5, No. 7, 2001, pp. 457–468.
doi:10.1016/S1270-9638(01)01123-3
- [42] Oseen, C. W., *Neuere Methoden und Ergebnisse in der Hydrodynamik*, Akademische Verlagsgesellschaft, Leipzig, Germany, 1927, pp. 82–87.
- [43] Oseen, C. W., “Über Wirbelbewegung in Einer Reibenden Flüssigkeit,” *Arkiv för Matematik, Astronomi och Fysik*, Vol. 7, 1911, pp. 1–13.
- [44] Hamel, G., “Spiralförmige Bewegungen zäher Flüssigkeiten,” *Jahresbericht der Deutschen Mathematiker-Vereinigung*, Vol. 25, Cambridge Univ. Press, Cambridge, U.K., 1917, pp. 34–60, <http://eudml.org/doc/145468>.
- [45] Lamb, H., *Hydrodynamics*, 6th ed., Cambridge Univ. Press, 1932, Chap. 11, S 334–a.
- [46] Ragab, S., and Sreedhar, M., “Numerical Simulation of Vortices with Axial Velocity Deficits,” *Physics of Fluids*, Vol. 7, No. 3, March 1995, pp. 549–558.
doi:10.1063/1.868582

C. Bailly
Associate Editor